Article

Giving New Life to Waste Cigarette Butts: Transformation into Platinum Group Metal-Free Electrocatalysts for Oxygen Reduction Reaction in Acid, Neutral and Alkaline Environment

Davide Testa [1,†], Giovanni Zuccante [1,†], Mohsin Muhyuddin [1,†], Roberto Landone [1], Axel Scommegna [1], Roberto Lorenzi [1], Maurizio Acciarri [1], Elisabetta Petri [2], Francesca Soavi [2], Lorenzo Poggini [3], Laura Capozzoli [3], Alessandro Lavacchi [3], Niccolò Lamanna [4], Andrea Franzetti [4], Luca Zoia [4] and Carlo Santoro [1,*]

[1] Department of Materials Science, University of Milano-Bicocca, U5 Via Cozzi 55, 20125 Milan, Italy
[2] Department of Chemistry "G. Ciamician", Alma Mater Studiorum University of Bologna, Via Selmi 2, 40100 Bologna, Italy
[3] Istituto di Chimica Dei Composti OrganoMetallici (ICCOM), Consiglio Nazionale Delle Ricerche (CNR), Via Madonna Del Piano 10, 50019 Sesto Fiorentino, Italy
[4] Department of Earth and Environmental Sciences, University of Milano-Bicocca, Building U01, Piazza della Scienza 1, 20126 Milan, Italy
[*] Correspondence: carlo.santoro@unimib.it
[†] These authors contributed equally to this work.

Abstract: Following the core theme of a circular economy, a novel strategy to upcycle cigarette butt waste into platinum group metal (PGM)-free metal nitrogen carbon (M-N-C) electrocatalysts for oxygen reduction reaction (ORR) is presented. The experimental route was composed of (i) the transformation of the powdered cigarette butts into carbonaceous char via pyrolysis at 450 °C, 600 °C, 750 °C and 900 °C, (ii) the porosity activation with KOH and (iii) the functionalization of the activated chars with iron (II) phthalocyanine (FePc). The electrochemical outcomes obtained by the rotating disk electrode (RRDE) technique revealed that the sample pyrolyzed at 450 °C (i.e., cig_450) outperformed the other counterparts with its highest onset (E_{on}) and half-wave potentials ($E_{1/2}$) and demonstrated nearly tetra-electronic ORR in acidic, neutral and alkaline electrolytes, all resulting from the optimal surface chemistry and textural properties.

Keywords: waste cigarettes; char; PGM-free; oxygen reduction reaction; electrocatalysis

1. Introduction

Daily solid waste production through industrial, agricultural and municipal sources accounts for 7 to 9 billion tons all around the world [1]. A major proportion of the waste biomass often ends up in landfills without being recycled, thus engendering severe challenges to environmental safety. Amid such a prevailing anxious situation, the circular economy introduces a concept to upgrade waste products into value-added materials which could be potentially employed for a broad spectrum of advanced applications. Unlike the linear economy, which leads to both depletion of raw materials and uncontrollable waste streams, the circular economy aims at minimizing the input of pristine sources and the output of wastes by looping materials flows [2,3]. Therefore, this economic approach can impressively benefit the industrial chain production of materials, which is affected by the ever-increasing price of earth sources and can save the costs associated with waste disposal and landfill maintenance.

Among the paramount non-recyclable wastes, cigarette butts represent a severe environmental threat as 5.7 trillion cigarettes are annually smoked around the globe while the figure is expected to reach 9 trillion by the year 2025 [4,5]. Regardless of the adverse effects of tobacco on human health, which killed 7 million individuals in 2020 [6], the dispersion of

extinguished cigarettes into the environment or landfills can further raise plastic pollution due to the presence of toxic and non-biodegradable cellulose acetate filters [7]. In fact, these litters contribute to plastic pollution as 300,000 tons of microplastic fibers from cigarette filters end up in the aquatic environment [8]. On top of that, cellulose acetate filters act as powerful vectors of several pollutants (e.g., Pb, Cd, PAHs, BTEX, aromatic amines) due to the strong adsorption capacity of the filter fibers, and these substances can be accidentally consumed along with microplastics by aquatic creatures [8–10]. Therefore, these catastrophic environmental consequences call for preventing cigarette butt accumulation, which can be fulfilled by adopting worthy solutions aiding the circular economy. In other words, this non-recyclable waste should be turned into value-added products, which can ensure environmental safeguards [11].

As a conventional practice, incineration could help in ceasing the mass accumulation of non-recyclable wastes which in turn also provides a limited fraction of energy. However, the considerable release of hazardous by-products into the atmosphere, such as dioxins [12], CO_2 [13], etc., is the major pitfall of such a pathway. In addition to land toxicity and water pollution, climate change, particularly due to the release of greenhouse gases (including CO, CO_2), is another alarming issue, demanding urgent solutions. The energy sector is one of the main CO_2 emitters as 84% of the global primary energy consumption derives from fossil fuel combustion [14].

In parallel, the expected extinction of fossil fuels and ecological concerns are encouraging the exploration of cleaner and renewable energy alternatives, such as solar [15], wind [16], ocean waves [17] and geothermal energies [18]. The efforts and progress made in this sense have raised the percentage of global primary energy consumption supplied by renewable sources up to 11.4% [14]. Nonetheless, it is worth mentioning that these energy sources suffer from intermittence, which requires the introduction of robust energy storage systems such as batteries to flatten their peaks of energy production [19]. On the other hand, the utilization of hydrogen as an energy vector is considered one of the future strategies. However, the sustainable transition to a hydrogen economy still faces several challenges mainly involving the production of green hydrogen and the safe transportation of hydrogen through solid infrastructures [20].

One of the rational applications of hydrogen as a fuel is surely low-temperature fuel cells (FCs), i.e., devices capable of converting the chemical energy of reactants (H_2 as fuel and O_2 as comburent) into clean electrical energy. From the electrocatalytic point of view, the cathodic reaction, oxygen reduction reaction (ORR), has sluggish kinetics compared to that of the anodic side, i.e., hydrogen oxidation reaction (HOR) [21]. Mostly, the ORR active electrocatalysts rely on nanosized platinum group metals (PGMs) [22,23]. Notwithstanding, they are exotic, scarce and expensive; moreover, their extraction is mainly restricted to a few geopolitically unstable regions [24]. Consequently, such economic incompatibilities hinder the large-scale commercialization of low-temperature FCs.

Hence, current research strives to find cheaper alternatives to PGMs by focusing on single-atom electrocatalysts containing earth-abundant first-row transition metals known as M-N-C type electrocatalysts, where M = Fe, Ni, Co, etc. [25,26]. These novel materials own actives sites composed of a metallic center coordinated by nitrogen atoms (i.e., MN_x, where x is 2, 3 and 4, depending on the material defectivity) moieties integrated into a carbon matrix [27]. One of the most active materials towards ORR are Fe-N-C, according to the most recent studies [28]. Despite the appreciable electrocatalytic performance of M-N-C, these electrocatalysts seem to be more stable in the alkaline environment of anion exchange membrane fuel cells (AEMFCs), which also favor the kinetics of ORR rather than the unbearable acid environment of proton exchange membrane fuel cells (PEMFCs), where the non-noble metal can be easily leached out of the carbon matrix. Moreover, Nafion® membrane used in PEMFCs, enabling proton conduction, is strongly pollutant due to the perfluoroalkyl components of the polymer [29,30]. Conversely, the most recent fluorine-free anion exchange non-porous membranes designed for alkaline fuel cells are less non-eco-friendly [31].

Another promising technology in the view of decarbonization is bioelectrochemical systems (BES) and particularly microbial fuel cells (MFCs). MFCs operate in a neutral environment to allow the operations of electroactive microorganisms at the anode [32]. These bacteria degrade organics and pollutants [33] and transfer the electrons to the anode electrodes producing electricity. At the cathode, a reduction reaction occurs where oxygen is the preferred electron acceptor [34]. Being the less developed technology and in parallel also the less performing in terms of power generation, MFCs inherit the materials from mainstream AEMFC and PEMFC [35]. Carbon-based materials, especially in the form of nanotubes, rods, sheets and foam, have gained great interest as MFC electrodes due to their conductivity, surface area, corrosion resistance and in most cases biocompatibility [36]. Due to these features, carbons have been exploited in electrochemical sensing as well as in electrocatalysis [37]. However, their energy performance is limited in the absence of metal centers [36]. Thus, also in MFCs, the best electrocatalytic activity for ORR is provided by M-N_x-C electrocatalysts being resilient, low cost and effective [38,39]. M-N_x-C-based cathodes are also effective in Direct Methanol Fuel Cells (DMFC) as they resist the OCV drop due to the fuel crossover which is a typical problem with PGM cathode electrocatalysts [40,41]. In the context of low-temperature FCs, several studies have supported the circular economy by developing novel synthetic pathways that can convert carbonaceous waste into PGM-free ORR electrocatalysts via pyrolysis [42–46]. Up to now, research is mainly inclined towards biomass-derived waste: orange peel [47], lignin [48,49], coconuts [50], chicken feathers [51], waste tea [52], sheep-horn [53], pistachio shells [54], etc. Meanwhile, some scientific articles have recently developed PGM-free electrocatalysts from scrap plastics, which are undoubtedly more critical because of their slow degradation [55–59]. Surprisingly, none have still used the widespread cigarette butts as a nearly zero-cost carbon precursor for the synthesis of PGM-free electrocatalysts; notwithstanding, some attempts to pyrolyze cigarette butts have already been made [60–62].

This work introduces cigarette butts as cost-effective and readily available carbon precursors for PGM-free electrocatalysts for ORR. The suitable range of temperature to achieve a char with desirable properties for electrocatalytic purposes (e.g., accessibility to active sites and electronic conductivity) usually spans between 400 and 1000 °C [63]. Above 400 °C, the majority of carbon precursors release gases that lead to the development of pores and variations in the surface chemistry with a decrease in the H/C and O/C ratios as temperature increases during pyrolysis. Subsequent graphitization and healing of structural defects also take place during the thermal treatment. Beyond 900–1000 °C, partial melting of some volatile fractions blocks pores, thus hindering the accessibility of reactant molecules to the active sites [64,65]. Considering all these aspects, the pristine cigarette butts were pyrolyzed at these four temperatures: 450 °C, 600 °C, 750 °C and 900 °C. The obtained materials were subsequently activated with KOH to achieve a high surface area to guarantee improved micro-mesoporous interconnectivity, which is essential for the transportation of reactant molecules toward the active sites. Ultimately, the activated carbons were functionalized by homogeneously mixing them with iron phthalocyanine, employed as a precursor for the creation of the actual electrocatalytic centers. The obtained electrocatalysts were tested via rotating ring disk electrode (RRDE) in acidic, neutral and alkaline environments to compare the material performance in terms of electrocatalytic activity and stability by varying the pyrolysis temperature. Overall, this study supports the vision of the aforementioned circular economy since a non-recyclable zero-cost waste (i.e., cigarette butts) alternatively predestined for landfills is turned into a valuable and promising low-cost material, which can potentially promote the commercialization of environmental-friendly energy converting devices, i.e., FCs.

2. Results and Discussion

Figure 1 schematically demonstrates the route followed for the synthesis of ORR electrocatalysts using waste cigarette butts as a carbon source where the details can be found in the experimental section. Blended cigarette butts were pyrolyzed at four different

temperatures specifically 450 °C, 600 °C, 750 °C and 900 °C after being ball-milled. The achieved chars were then activated with KOH to induce porosity and achieve a higher surface area. Eventually, the ORR electrocatalysts were fabricated by functionalizing the different activated chars with iron (II) phthalocyanine (FePc) to launch ORR active sites in the carbonaceous framework. Afterward, the electrocatalysts were thoroughly characterized to study the relationship between the performance and structural parameters. The final samples were labeled as cig_450, cig_600, cig_750 and cig_900, according to the temperature set in the first pyrolysis treatment. To compare the chemical changes before and after pyrolysis treatment, the only ball-milled sample, labeled as cig_BM, was also considered in some analyses. The detailed procedure for the sample preparation is precisely described in the experimental section.
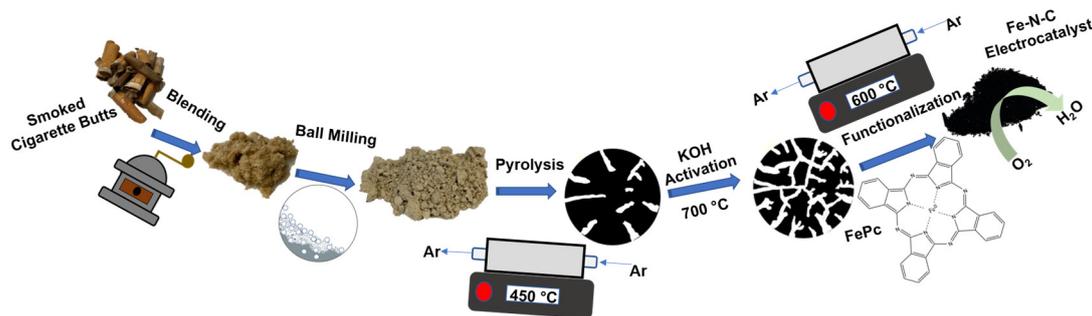
Figure 1. The synthesis scheme of the ORR electrocatalysts prepared in this work.

2.1. Structural and Morphological Results

First of all, the thermal profile of the raw material, i.e., cig_BM, was studied through thermogravimetric analysis (TGA) in N_2 atmosphere to trace the structural evaluation in the char formation during pyrolysis, and the achieved trend is reported in Figure S1. Cig_BM showed thermal behavior similar to that reported by S. Yousef et al. [66]. The first decrease in weight occurs between 150 and 200 °C due to the evaporation of moisture and volatile chemical residues remaining from the manufacturing stages. A further increase in temperature (up to 280 °C) results in the breaking down of the chemical bonds between all components of the cigarette, i.e., filter, tobacco and paper [66]. Subsequently, the material enters the main decomposition zone (280–370 °C) where compounds such as acetic acid and phenol result from the decomposition of bigger molecules with low crystallinity. Moreover, some small molecules can react and join together upon applied heating, thus creating new chemical compounds, such as propanone, limonene and pyridine [66]. After the evaporation of all gaseous byproducts, the small leftover solid mass (<25%) remains almost constant upon heating, which confirms the generation of char. It is worth mentioning that eventually the char production becomes completed well before 450 °C. To investigate the inorganic constituents of the samples, XRF was performed, and the results are reported in Figure S2a–e (Supplementary material). All the samples exhibited impurity signals from Ca, K and Ti which were originally present in the raw cigarette butts in addition to Fe as demonstrated by the XRF spectra of cig_BM (Figure S2a). However, after functionalization with FePc, the peak corresponding to Fe became significantly intensified. Ca was present as a major impurity that could become involved from $CaCO_3$ which is normally added in cigarette papers to make the ash attractive during the burning of cigarettes [67]. On the other hand, the K signals might belong to potassium sorbate or potassium citrate which are usually added to the paper as combustion aid or preservatives [62,68,69]. The presence of Ti can be attributed to the TiO_2 commonly present in the cellulose acetate filter as TiO_2 bestows a white color and considerably reduces the content of hazardous chemicals that can be inhaled by smokers [67].

The crystallographic details of the samples were evaluated by employing XRD, and the obtained diffraction patterns are demonstrated in Figure 2a whereas the diffraction

pattern of the non-pyrolyzed sample cig_BM is additionally provided in Figure S2f. The XRD pattern of cig_BM indicated the co-presence of carbon and $CaCO_3$ as major phases present. Categorically intense peaks located at the 2θ position of ca. $14.8°$, $16.6°$ and $22.8°$ came out to be consistent with JCPDS card no. 00–050–0926 of hexagonal carbon. Moreover, the peaks located nearly at $29.5°$, $34.64°$, $35.86°$, $39.54°$, $43.28°$, $47.64°$, $48.6°$ and $57.2°$ were corresponded to $CaCO_3$ with JCPDS card no. 01–085–1108. Such results are consistent with the XRF studies. Quite interestingly, the functionalized samples did not show any apparent peak of $CaCO_3$ indicating its considerable removal during HCl washing treatments. On the other hand, the diffraction patterns of functionalized samples mainly depicted two characteristic broader peaks of defective carbon at ca. $25°$ and ca. $44°$ that correspond to the (002) and (100) graphite planes, respectively [70]. Additionally, low-intensity peaks at ca. $33°$, $45°$, $47.36°$, $59°$ and $79.3°$ can be ascribed to Fe_2O_3 (JCPDS no. 00-039-0238) which appeared in the case of cig_750, cig_900 and cig_450 [71].
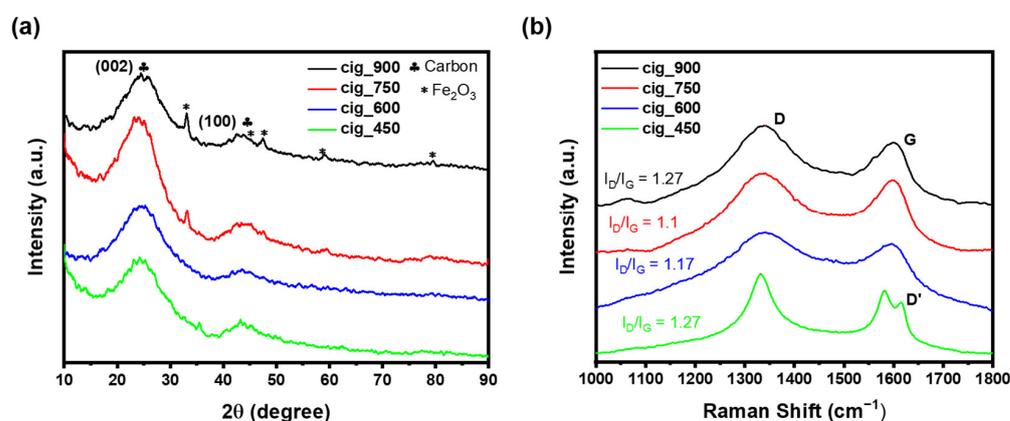

Figure 2. (**a**) XRD spectra and (**b**) Raman spectra of the as-prepared samples.

Raman spectroscopy was employed as one of the fundamental methods to explore the carbonaceous architecture of the derived electrocatalysts, and the acquired spectra are presented in Figure 2b. Graphitic materials are primarily composed of sp^2 hybridized hexagonal networks of C atoms having strong covalent bonding within the plane and weak Van der Waals interactions between the layers [72]. However, perfect graphitic materials hardly exist while practical carbon-based materials contain various kinds of structural defects which also contribute to uplifting the specific properties of interest. For the ORR activity edge defects act as the oxygen-binding moieties owing to dangling bonds [73] whereas graphitization is considered important to ensure electronic conductivity during electrocatalysis [74]. At the initial glance, all the electrocatalysts exhibited typical Raman features of the defective carbons, predominantly consisting of two main peaks i.e., D band and G band at the closed vicinity of 1330 cm^{-1} and 1590 cm^{-1}, respectively. G band is observed due to electron–phonon couplings in E_{2g} representation of Raman active modes where in-plane sp^2 bond-stretching of C atoms takes place while the D band emerges because of A_{1g} breathing symmetry. The perfect sp^2 carbon demonstrates only the G band whereas the structural defects give rise to the D and D′ bands [75]. To quantify the defect density in carbon-based materials, the intensity ratio of the D to G band (I_D/I_G), calculated from peak heights, is used as a common indicator. Moreover, the spectra have been fitting as a sum of asymmetric Breit–Wigner–Fano (BWF) bands, and the results are reported in Table S1 [76]. Interestingly, cig_450 exhibited a very sharp D peak, of about 46 cm^{-1}, along with a categorical D′ band present on the right shoulder of the G band at ca. 1615 cm^{-1}, indicating a defect-rich structure with an I_D/I_G value of 1.27. In the subsequent samples the band D′ vanished; the I_D/I_G decreased to 1.17 and then 1.10 in the case of cig_600 and cig_750, respectively. At 600 °C we also register a very large D peak with a width of 125 cm^{-1} indicating the formation of clusters with a broader distribution of dimensions and amorphousness [77]. At 750 °C and 900 °C, the pyrolysis leads to a further

rearrangement of amorphous carbon, and the D peak width is about 85 cm^{-1}, a value intermediate between cig_450 and cig_600. Finally, the sample cig_900 again demonstrated the relatively prominent D band, and the I_D/I_G ratio again approached 1.27.

The topographical and morphological analysis began with scanning electron microscopy (SEM) in the secondary electron (SE) mode, and the achieved micrographs of cig_450, cig_600 and cig_900 are illustrated in Figure S3. Apparently, the samples were agglomerated into nearly spherical globules with rough surfaces at the submicron level. However, to further figure out the morphological parameters, a transmission electron microscope (TEM) was employed. Figure 3 reports the TEM images for the samples of cig_450 and cig_750. The data relating to the samples of cig_600 and cig_900 are reported in the supplementary info section (Figure S4). The low and high-magnification HRTEM images of all the samples show no significant differences in the morphology (Figure 3a,b,e,f). This is confirmed by the HAADF images (Figure 3c,g). The EDX maps show that iron is distributed homogeneously in the material, with some accumulation in particles that are especially visible in the cig_750 sample (Figure 3d,h). The nanoparticles consist of iron oxides that were also identified as Fe_2O_3 by XRD as discussed above. As already identified with XRF, EDX spectra also show the occurrence of Ca (also shown in the EDX maps), Ti, Mg and Si.

Surface chemistry is particularly relevant to gain a deep understanding of the reactions which occur on an electrocatalyst surface such as ORR. Herein, the surface chemistry of the pyrolyzed samples was studied by XPS. The survey scans of Figure S5 depict the predominance of carbon and oxygen, as highly intense C1*s* and O1*s* peaks are detected at 286 and 532 eV of binding energy (BE). Tiny peaks belonging to N1*s* and Fe2*p* appear at the 400 and 720 eV. Table S2 reports the relative at% quantities of N and Fe for cig_450, cig_600, cig_750 and cig_900. The content of Fe is between 0.2 and 0.3%. The nitrogen concentration oscillates between 1.3 and 2.0%, where the minimum is reached for cig_600 while the maximum is for cig_750.

Nitrogen plays a pivotal role in the activity along with the selectivity of ORR conducted with M-N-Cs [48,78,79]. Therefore, N1*s* high-resolution spectra of the cigarette butt-derived carbons were accurately investigated and reported in Figure 4a–d. The N1*s* signal spans 396–407 eV, and it was deconvoluted into six peaks at 397.1, 398.3, 399.6, 401.3, 403.4 and 405.6 eV corresponding to imine N, pyridinic N, Fe-N$_x$, hydrogenated N (including pyrrolic and hydrogenated pyridine), graphitic/protonated N (including quaternary nitrogen and protonated pyridine) and N-oxides (NO$_x$) nitrogen, respectively [80].

Figure S6 shows the relative % component ratio of every nitrogen moiety appearing in Figure 4a–d. Interestingly, nitrogen mainly appears as M-N$_x$, which corresponds to more than 40% for the pyrolyzed sample, reaching up to 45.3% for cig_450. The only exception is represented by cig_750, whose M-N$_x$ concentration is tremendously inferior to that detected for the other samples. Moving on to the other types of N, all electrocatalysts display almost the same amount of imine N, pyridinic N, graphitic N and NO$_x$. Actually, cig_900 shows a slightly lower concentration of imine and pyridinic N with respect to the other samples, i.e., 5.4% vs. ca. 8–9% and 15.3% vs. 18–20%.
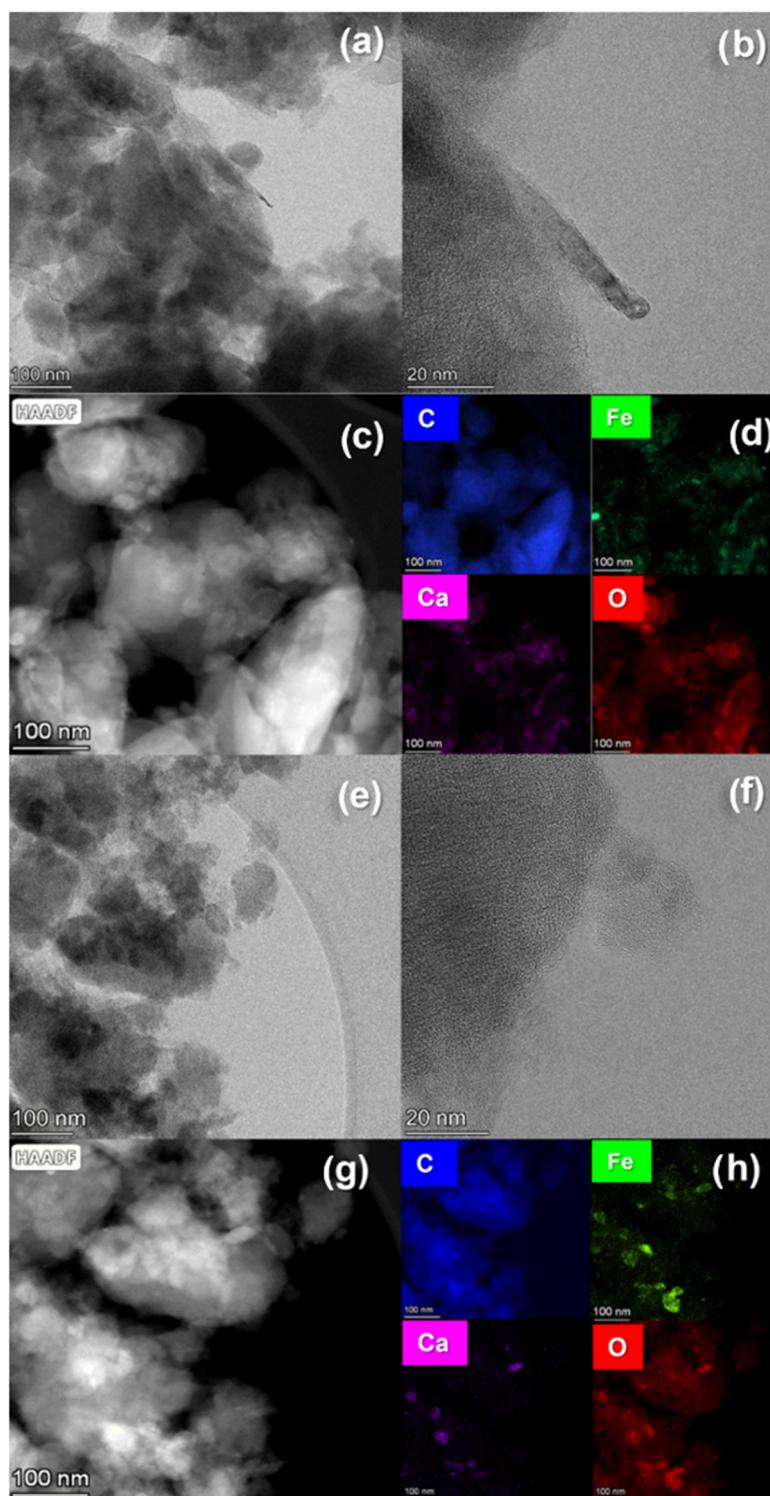
Figure 3. Electron microscopy investigation of cig_450 (**a–d**) and cig_750 (**e–h**). Low magnification HRTEM (**a**,**e**); high magnification HRTEM image (**b**,**f**); HAADF images (**c**,**g**); EDX maps of C, Fe, Ca and O (**d**,**h**).
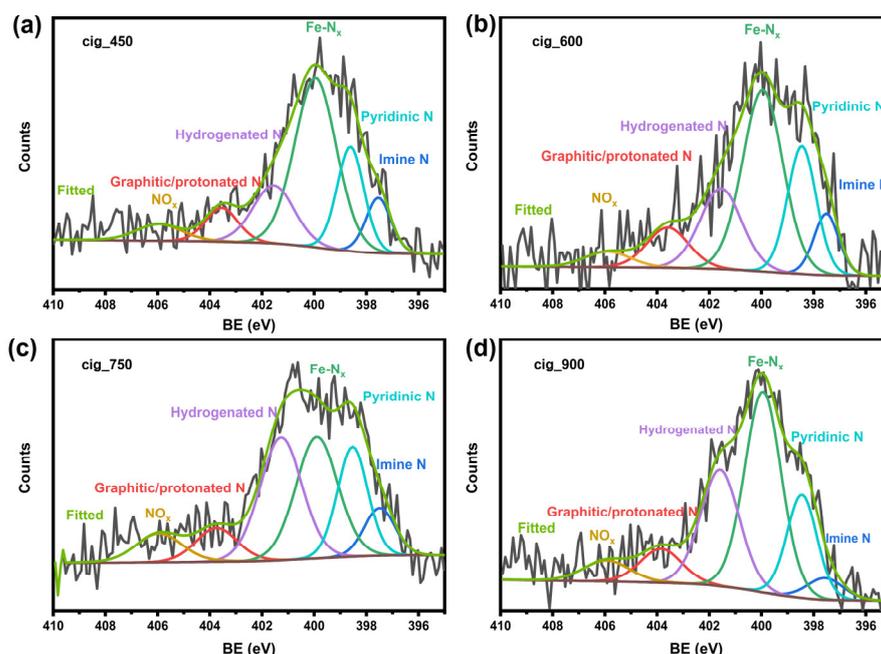
Figure 4. XPS deconvolution of N 1s peak of (**a**) cig_450, (**b**) cig_600, (**c**) cig_750 and (**d**) cig_900 with raw data.

Additionally, a tiny difference is observed for NO_x amount, which is slightly higher in the case of cig_750 compared to the other samples, i.e., 8% vs. 4–5%. On the other hand, hydrogenated N concentration strongly varies with the first pyrolysis temperature as its values are 15.3, 18.4, 23.7 and 28.9% for cig_450, cig_600, cig_900 and cig_750, respectively. Noteworthily, the co-existence of different nitrogen species on the carbon backbone is fundamental to determining the ORR performance [78,81]. It seems that every nitrogen moiety carries out a specific task during ORR [79,82]. It is commonly accepted that $Fe-N_x$ moieties play an essential role in addressing the ORR towards either a direct 4-electrons pathway, which leads to the H_2O formation, or the 2×2-electrons pathway, which proceeds with the subsequent conversion of peroxide into H_2O [79]. Instead, the metal-free nitrogen moieties seem to catalyze either the 2-electrons pathway, which engenders the unwanted hydrogen peroxide H_2O_2 in acidic media or peroxihydroxyl ion OH_2^- in alkaline media or the 2×2-electrons pathway [82]. For instance, hydrogenated-N moieties together with the graphitic-N moieties are likely to induce the incomplete reduction of oxygen to peroxide formation [81–83]. On the contrary, pyridinic and graphitic moieties may promote the second step of 2×2-electrons of ORR, i.e., H_2O_2 or OH_2^- reduction to water in an acidic and alkaline environment, respectively [82]. Furthermore, nitrogen moieties are pH-sensitive, which means that the reactivity of the active sites can vary accordingly. To provide an example, the calculated dissociation constant pK_a of pyridinic-N in doped graphene is about 6.5, which means that the majority of pyridinic-N is supposed to be protonated at lower pH, whereas it should be deprotonated at higher pH, especially in alkaline conditions [84]. This deprotonation of the pyridinic group leads to the formation of N^- Lewis base that favors the adsorption of O_2 [79]. In two different works, it was shown that PGM-free M-N-C type electrocatalysts follow the acid pathway when pH is around 10–11, which corresponds to the pK_a of the peroxide [84,85].

The high-resolution spectra of the C1*s* signal are reported in Figure S7, and it was deconvoluted in five peaks. The three peaks detected at lower BE, i.e., 284, 284.7 and 286 eV, refer to graphitic C (i.e., sp^2 hybridized carbon), amorphous C (i.e., sp^3 hybridized carbon) and C-N, respectively, whereas the last two peaks at 287.6 and 289.2 are related to C_xO_y species (i.e., C-O and C=O moieties) [86,87]. The appearance of carbon oxygenated species as well as C-N implies that the defectivity of the pyrolyzed samples, which was previously

unraveled by Raman spectroscopy through the appearance of D and D' bands, is due to the occurrence of both nitrogen and oxygen functional groups on the carbon surface.

The electrochemical performance is intimately connected to the morphological properties of hierarchical mesoporous carbons. A highly porous material permits a better exposition of the active sites where the reaction can occur. To achieve tremendous specific surface areas and pore volumes, the material should be mostly micro and mesoporous. As a matter of fact, micropores favor the hosting of M-N_x active sites, while mesopores mostly allow conveying of the reactants to the active sites [88]. Therefore, the absence of mesopores signifies that a large part of the physical surface area cannot be reached by reactants since diffusion is hindered. Herein, the textural properties were evaluated by recording the N_2 adsorption/desorption isotherms at 77 K, reported in Figure 5a. To obtain the specific surface area (SSA) and the pore size distribution (PSD), the Brunauer–Emmett–Teller method (BET) and density functional theories (DFT) were adopted for the isotherm analysis.
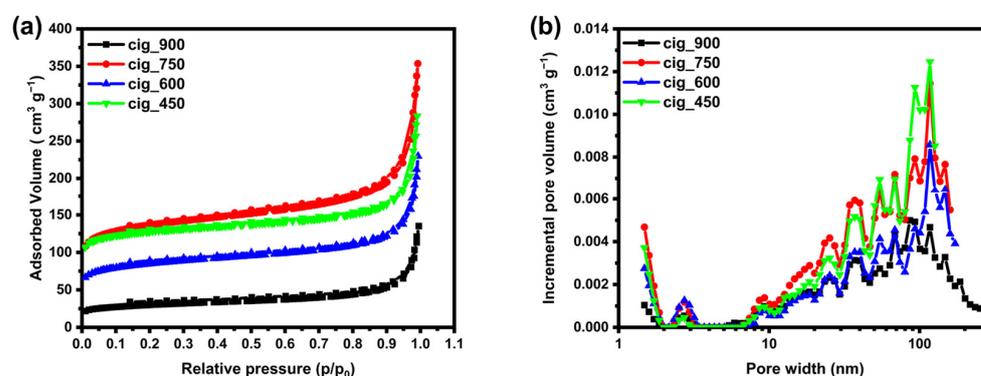
Figure 5. N_2 adsorption–desorption isotherms (**a**) and pore size distribution (**b**) of the four tested electrocatalysts.

Remarkably, cig_750 and cig_450 show similar adsorptive capabilities, which are more accentuated than cig_600 and cig_900. The adsorption uptake at small relative pressures (p/p_0) gives rise to a shape compatible with type I isotherms, indicating the presence of micropores in the material. The steeper the uptake at low p/p_0, the larger the number of micropores. At p/p_0 values superior to 0.8, the curves resemble a type IV isotherm, which entails the presence of mesopores and macropores when the isotherm sharply increases. These observations are confirmed by DFT pore size distribution (PSD) represented in Figure 5b and by the data summarized in Table 1, which include BET surface area (S_{BET}), micropore, mesopore and total volume (V_{micro}, V_{meso} and V_{tot}, respectively). For each electrocatalyst, the pore size distribution shows a small peak between 2 and 3 nm, but the main pore size spans between 8 nm and 100 nm. More specifically, the PSD of cig_450 and cig_750 follow the same trend within the microporous and mesoporous region up to ca. 50 nm; beyond that number, the PSD of cig_450 depicts the topmost value. On the contrary, cig_600 and mostly cig_900 reach low incremental pore volume values, signifying lesser porosity. This statement is fairly consistent with the values reported in Table 1, where cig_900 displays much lower S_{BET} and V_{micro}, V_{meso} compared to the other electrocatalysts. In cig_450, cig_600 and cig_750, micropores are the most contributors to V_{tot} since V_{micro} is twice as V_{meso}. Consequently, the obtained materials are mostly microporous. In general, it is worth mentioning that such S_{BET}, V_{micro}, and V_{meso} numbers resulted from an effective activation process, which aimed at increasing the micropososity and mesoporosity. It is not possible to individuate a trend of S_{BET} and V_{tot} with the pyrolysis temperature, but cig_450 and cig_750 are likely to feature the highest surface area, i.e., 448.83 m^2 g^{-1} and 513.45 m^2 g^{-1}, respectively, and total pore volume, i.e., 0.31 and 0.32 cm^3 g^{-1}. The S_{BET} values reported in this work are high enough to allow a good electrocatalytic activity [89]. However, it should be mentioned that the S_{BET} and V_{meso} values are lower compared to

the KOH-activated Fe-N-C electrocatalysts reported in other works (which can reach even 1000 m^2 g^{-1} and 0.5 cm^3 g^{-1}) [90–92].

Table 1. BET specific surface area (S_{BET}), micropores volume (V_{micro}), mesopore volume (V_{meso}) and total pore volume (V_{total}) of the different samples.

| Sample	S_{BET} [m^2 g^{-1}]	V_{micro} [cm^3 g^{-1}]	V_{meso} [cm^3 g^{-1}]	V_{total} [cm^3 g^{-1}]
cig_450	490	0.15	0.06	0.31 (<127 nm)
cig_600	317	0.09	0.05	0.21 (<172 nm)
cig_750	513	0.14	0.08	0.32 (<179 nm)
cig_900	110	0.03	0.05	0.13 (<273 nm)

2.2. Electrochemical Performance of the Cigarette-Butt-Derived Electrocatalysts

To evaluate the electrochemical activity of the cigarette butt-derived electrocatalysts, linear sweep voltammograms (LSVs) were acquired at 5 mV s^{-1} using RRDE as a working electrode rotating at 1600 rpm. Three different oxygen-saturated electrolytes: acidic (0.5 M H$_2$SO$_4$), neutral (0.1 potassium phosphate buffer, PBS) and alkaline (0.1 M KOH) were employed since the mechanism of ORR changes according to the pH of the electrolyte [84,93]. Unlike the rotating disk electrode (RDE), RRDE is a reversible mass transfer technique: oxygen is reduced to H$_2$O (4-electrons pathway) or H$_2$O$_2$ (2-electrons pathway) on the disk surface, and the reduced species are oxidized to O$_2$ back on the ring surface. Therefore, RRDE produces two types of current: disk current (J_{disk}) and ring current (J_{ring}) [94]. The disk current results from the reduction reaction whereas the ring current is obtained from the oxidation reaction (in our experiments). The onset potential (E_{on}), the half-wave potential ($E_{1/2}$) and the diffusion limiting current density (J_{lim}) are the commonly used parameters to compare the activity of different electrocatalysts [94]. Instead, the hydrogen peroxide yield and the electron transfer number justify the utilization of electrocatalysts for practical applications in fuel cells, where hydrogen peroxide can potentially destroy the operating membrane [95]. In this study, E_{on} was estimated at −0.1 mA cm^{-2} current density whereas $E_{1/2}$ was determined by taking the first derivative of the obtained LSVs.

2.2.1. Electrocatalytic Activity in Acidic Media

Carrying out RRDE measurements of M-N-C electrocatalysts in acidic media is extremely important to reveal their potential application as a replacement for PGMs in PEMFCs [24,96]. Figure 6a–d compares the electrochemical results achieved for the electrocatalysts synthesized by changing the temperature of the first pyrolysis, which aimed at converting the waste precursor (cigarette butts) into carbonaceous char. By starting from the LSVs of the disk current reported in Figure 6a, it is worth observing that the LSVs do not show a limiting current plateau at low potentials (<0.3 V vs. RHE), which is indicative of a diffusion-controlled mechanism, but the LSV tail seems to change the slope. This means that the system is still controlled by both kinetics and diffusion at low potentials. In the case of cig_900, however, the typical sigmoidal shape of LSV is not detected, and the current density is much smaller than that shown by the other electrocatalyst, which is an indication of limited ORR activity. Conversely, the electrocatalyst pyrolyzed at cig_450 is the most active in terms of output J_{disk} and J_{ring} current at equal potential. In fact, cig_450 performs outstandingly by demonstrating E_{on} and $E_{1/2}$ of 0.877 V vs. RHE and 0.682 V vs. RHE, respectively, which are higher than those of other counterparts as reported in Table 2. Interestingly, Figure S8a shows a linear trend (with a correlation coefficient R^2 near 1) correlating the $E_{1/2}$ of the disk LSVs and the pyrolysis temperature. According to this plot, $E_{1/2}$ decreases by raising the pyrolysis temperature. Since $E_{1/2}$ is an indicator of the electrocatalytic performance, it can be concluded that the activity of the iron-functionalized samples follows this trend cig_450 > cig_600 > cig_750 > cig_900. Considering the current reached in the limiting current regime at low potential (0.2 V), cig_450 beats the other counterparts by far with a current density of −3.25 mA cm^{-2}. This number is similar to

that achieved by some of the commercial Fe-N-C electrocatalysts tested with a loading of 0.2 mg cm^{-2} in the Prins et al. study [97].
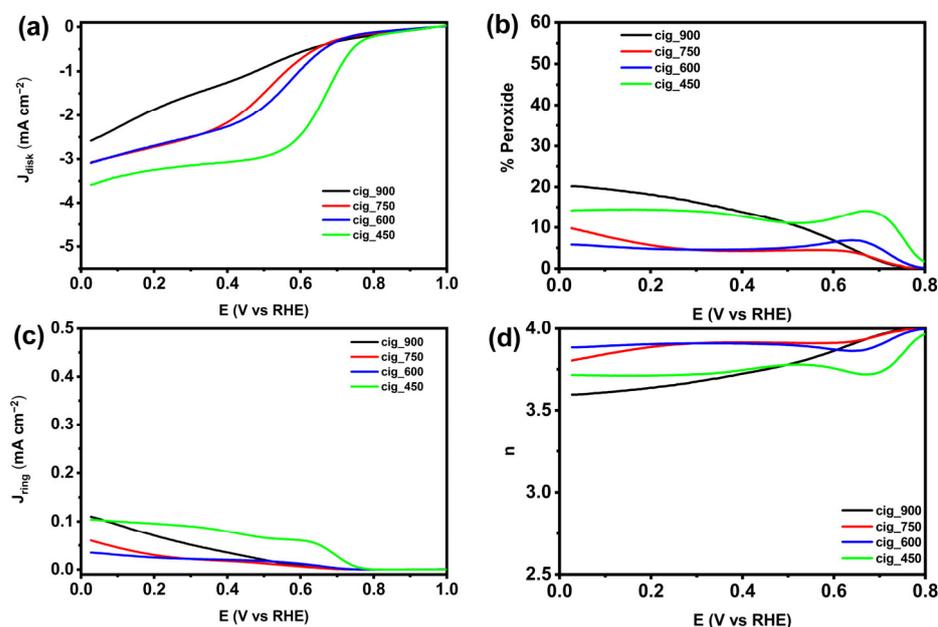
Figure 6. RRDE results of the samples in acidic media: (**a**) Disk current density (J_{disk}) and (**c**) Ring current density (J_{ring}) recorded at 1600 rpm and 5 mV s^{-1}, (**b**) % Peroxide and (**d**) the number of transferred electrons (n).

Table 2. Electrochemical data of the samples in the tested electrolyte.

	Acid		Neutral		Alkaline	
Sample	E_{on} [V vs. RHE]	$E_{1/2}$ [V vs. RHE]	E_{on} [V vs. RHE]	$E_{1/2}$ [V vs. RHE]	E_{on} [V vs. RHE]	$E_{1/2}$ [V vs. RHE]
cig_900	0.88	0.50	0.73	0.41	0.88	0.76
cig_750	0.86	0.53	0.71	0.37	0.86	0.79
cig_600	0.83	0.59	0.73	0.37	0.88	0.81
cig_450	0.88	0.68	0.77	0.43	0.91	0.85

E_{on} stands for onset potential; $E_{1/2}$ stands for half-wave potential.

Hydrogen peroxide production (Figure 6b) remains below 20% displaying some distinctions among electrocatalysts. Cig_600 and cig_750 are the most efficient electrocatalysts as peroxide yield is inferior to 10%, contrary to cig_450 and cig_900 which depict H_2O_2 percentages up to 15 and 20%, respectively. Importantly, the quantity of H_2O_2 produced affects the current engendered at the ring J_{ring} illustrated in Figure 6c: the more H_2O_2 forms the greater the resultant J_{ring}.

Although the production of H_2O_2 is relatively high compared to M-N-C electrocatalysts synthesized in other works [58,98], the number of transferred electrons ranges between 3.6 and 4.0 (Figure 6d), thus highlighting that the synthesized (and functionalized) electrocatalysts are more selective to the 4 or 2 × 2-electrons pathway, which leads to the water production.

2.2.2. Electrocatalytic Activity in Neutral Media

Evaluating the activity of the iron-functionalized electrocatalysts in a neutral environment provides insights for the implementations in MFCs, where the polluted water can be used for power generation by exploiting microorganisms [99,100]. The neutral and polluting environment of MFCs deactivates the PGMs, and hence, a logic to technologically

design non-PGMs electrocatalysts prevails [101,102]. With this intention, the activity of the developed electrocatalysts was assessed by RRDE in neutral media (0.1 M PBS). The LSVs obtained from the ring and disk current are shown in Figure 7a,c, respectively, whereas the trends in hydrogen peroxide production and the number of transferred electrons are illustrated in Figure 7b,d, respectively. Table 2 provides the values of E_{on} and $E_{1/2}$ obtained for each electrocatalyst in the neutral media. The estimated E_{on} and $E_{1/2}$ are lower compared to the acidic case, thus depicting hindered kinetics due to a reduced concentration (10^{-7} M) of H^+ and OH^- ionic species [103]. E_{on} values reported in Table 2 follow the trend cig_450 > cig_900 > cig_750 > cig_600.
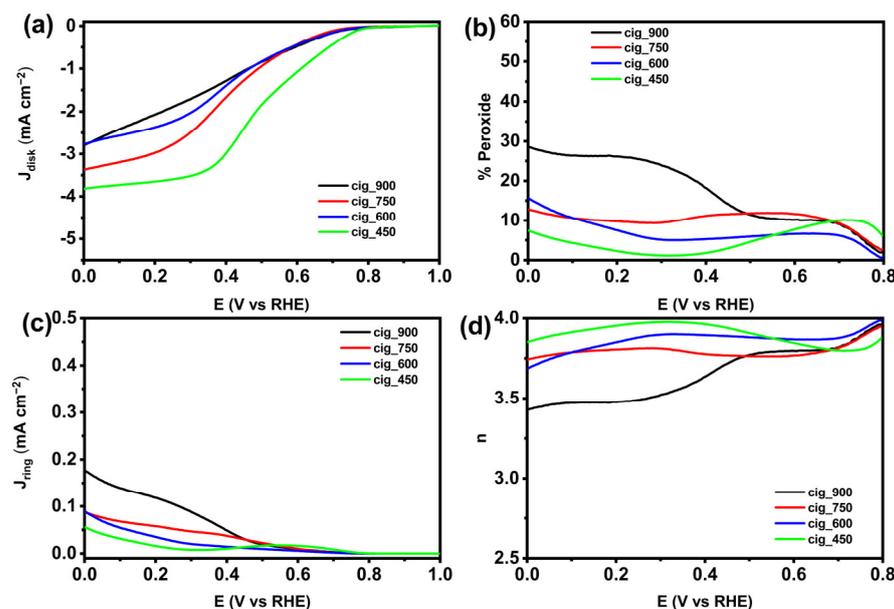
Figure 7. RRDE results of samples in neutral media: (**a**) Disk current density (J_{disk}) and (**c**) Ring current density (J_{ring}) recorded at 1600 rpm and 5 mV s^{-1}, (**b**) % Peroxide and (**d**) the number of transferred electrons (n).

Moreover, cig_600 and cig_700 demonstrate almost equal $E_{1/2}$ whereas $E_{1/2}$ reaches a peak in the case of cig_450. As reported in Figure S8c, $E_{1/2}$ does not show a specific trend with pyrolysis temperature in the neutral environment, unlike the acidic case (and alkaline which will be discussed in the subsequent section).

Apart from cig_450, the limiting current plateau struggles to be reached at low potential, thus implying that the electrochemical system is controlled by both diffusion and kinetics. Considering E_{on}, $E_{1/2}$ and the current attained at low potentials, it can be concluded that the electrocatalytic activity follows this descending trend: cig_450 > cig_750 > cig_900 $\cong$ cig_600. While again outperforming the other samples, cig_450 demonstrated 0.771 V vs. RHE in neutral media.

In Figure 7b, H_2O_2 yield rises to more elevated values with respect to the acidic media by arriving at 27% at 0 V vs. RHE in the case of cig_900. Herein, cig_450 releases a smaller amount of H_2O_2 compared to the other catalysts achieving a maximum of 9% yield at 0.7 V vs. RHE, which is indeed smaller than the value detected in the acidic situation (i.e., 15%). The results achieved for H_2O_2 reflect the number of transferred electrons n displayed in Figure 7d. The n values fluctuate around 3.8 for cig_450, cig_600 and cig_750, while they decline up to 3.4 for cig_900 at low potentials. Apart from these tiny differences, n overall remains large enough (i.e., 3.4–3.95) to validate the 4 or 2 × 2-electron pathway of ORR even in neutral media.

2.2.3. Electrocatalytic Activity in Alkaline Media

The alkaline environment favors the ORR performance of M-N-C electrocatalysts with respect to acid and neutral media. In fact, a well-designed M-N-C electrocatalyst can perform even better than Pt/C electrocatalysts, thus encouraging the replacement of these expensive materials with much cheaper alternatives in AEMFCs [52,104,105]. Hereinafter, the ORR activity of the obtained iron-functionalized electrocatalyst is tested in a 0.1 M KOH electrolyte, and results are reported in Figure 8a–d. Importantly, the J_{disk} LSVs of Figure 8a depict a reduced overpotential for all electrocatalysts compared to acid and neutral electrolytes. Consequently, it turns out that the E_{on} and $E_{1/2}$ are more positive in the alkaline media. More specifically, E_{on} values range between 0.861 and 0.911 V vs. RHE while the corresponding $E_{1/2}$ ranges between 0.761 and 0.850 V vs. RHE (Table 2). Such elevated activities in alkaline media might result from a partial contribution of the alkaline peroxide intermediate OH_2^- (predominant at pH > 12 [106]), which has superior stability on Fe^{2+} active sites compared to the acidic intermediate H_2O_2 [107]. Interestingly, Figure S8b displays the same linear relationship between $E_{1/2}$ and the first pyrolysis temperature observed in the acidic environment (Figure S8a); i.e., the higher the heat treatment temperature, the lower the achieved $E_{1/2}$. In other words, the activity estimated by $E_{1/2}$ is affected by synthetic conditions, and it declines linearly with temperature. This outstanding achievement opens a novel way of designing active M-N-C electrocatalysts as the electrochemical properties can be correlated to the synthetic conditions. The peroxide (Figure 8b) of alkaline media overcomes the values obtained in acidic and neutral media since it reaches up to 50% for cig_900. This implies that the amount of peroxide produced is pH-sensitive [58]. In their article, the production of peroxide for the waste-polyurethane-derived Fe-N-C electrocatalysts moves from 5% to 60% by varying the pH from 1 to 13 [58]. Such elevated yields of peroxide are primarily due to the predominance of the outer-sphere electron transfer mechanism occurring in the alkaline environment, which seems to privilege the 2-electron peroxide intermediate as the ultimate product [108]. The largest amount of peroxide is achieved between 0.5 and 0.7 V vs. RHE, and the maximum position strictly depends on the nature of the electrocatalyst. The tendency of peroxide percentage influences the ring current curve (Figure 8c), which sharply increases between 0.7 and 0.8 V vs. RHE and achieves a maximum at 0.5 V vs. RHE corresponding to a heightened development of peroxide. The more peroxide that is produced the higher the attained ring current. Noticeably, the J_{ring} decrease in cig_900 at lower potential is likely associated with the reduction of the peroxide intermediate OH_2^- to OH^-, which is the final product of the tetra-electronic process in alkaline media. This signifies that the ORR mechanism is not a direct 4-electrons transfer but a 2 × 2-electrons pathway; namely, O_2 is initially reduced to OH_2^-, and the peroxide intermediate is further reduced to OH^- [58,109]. The presence of a two-step reduction might explain the shape of the resulting LSVs, which seem to be composed of a first LSV at the upper potential and a second LSV at the lower potential. According to the previous literature works [54,58,110,111], the former might be associated with the first 2-electrons transfer from O_2 to OH_2^- while the latter might be related to the second 2-electrons transfer from OH_2^- to OH^-. The existence of a 2-electrons or a 2 × 2-electrons mechanism, instead of a straightforward 4-electrons mechanism, might explain why n of cig_900 firstly reaches a minimum of three electrons at 0.6 V vs. RHE (Figure 8d) and then rises to 3.6 electrons. In any case, focusing on the n values achieved at low potentials (0 V vs. RHE), the reduction process remains tetra-electronic in alkaline media as n is above 3.2.
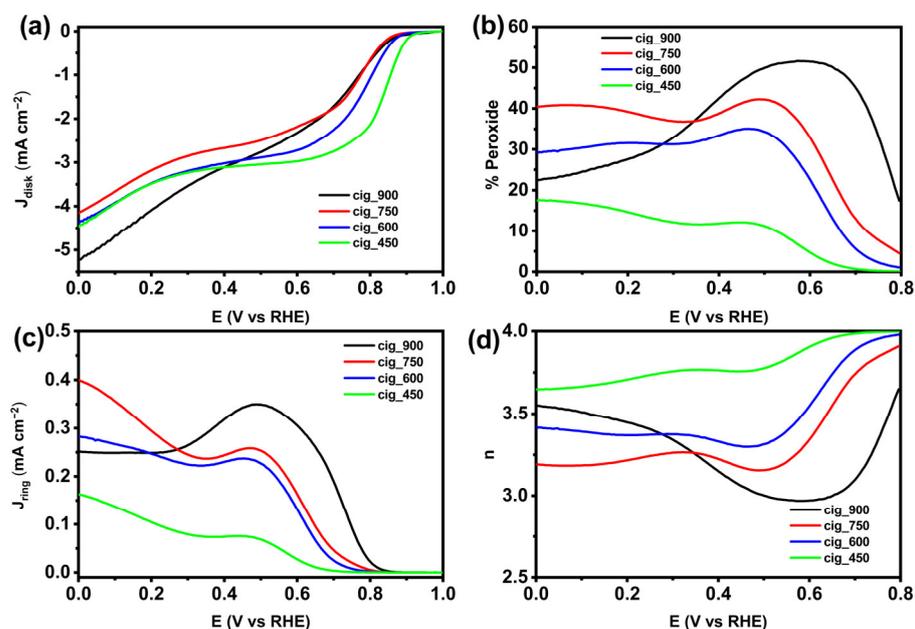
Figure 8. RRDE results of the samples conducted in alkaline media: (**a**) Disk current density (J_{disk}) and (**c**) Ring current density (J_{ring}) recorded at 1600 rpm and 5 mV s^{-1}, (**b**) % Peroxide yield and (**d**) the number of transferred electrons (n).

Regardless of the electrolyte pH, 450 °C is the topmost pyrolysis temperature to attain the best results from the activity point of view. Conversely, pyrolyzing cigarette butts at 900 °C results in a poorly performing electrocatalyst. Moreover, cig_450 exhibits a lower production of peroxide species in the alkaline media, which is quite close to the acidic one, compared to the other electrocatalysts. This finding might be ascribed to the occurrence of graphitic and hydrogenated nitrogen moieties, which are more abundant in cig_750 and cig_900, the highest peroxide producers in alkaline media. On top of that, a diminished amount of pyridinic moieties in cig_900 compared to the other samples could further enhance peroxide production since pyridinic N is hypothesized to reduce peroxide species in water [82]. Importantly, cig_900 and cig_450 have the same defectivity ($I_D/I_G = 1.27$) and a similar abundance of Fe-N$_x$ moieties which prompt the ORR. Notwithstanding, the lack of porosity of cig_900 witnessed by the low surface area and pore volume of 109 m^2 g^{-1} and 0.133 cm^3 g^{-1}, respectively, makes its kinetics particularly sluggish compared to the other electrocatalysts. As aforementioned, pores allow the reactant molecules to reach the internal active sites, thus increasing the resultant current density [86]. Hence, scarce porosity hinders the accessibility to active sites, thus terribly affecting the reaction kinetics [88]. Interestingly, cig_750 displays a minutely higher surface area and pore volume with respect to cig_450 (see Table 1). However, cig_750 shows a much less abundance of Fe-N$_x$ and a much higher amount of hydrogenated N moieties, which leads to a decreased performance in terms of electrocatalytic selectivity and activity. To summarize, the outstanding performance of cig_450 results from a trade-off between its great surface area and the amount of homogeneously distributed Fe-N$_x$ moieties, whose number is superior to that of the other electrocatalysts. As a final consideration, the $E_{1/2}$ of 0.85 V vs. RHE achieved by cig_450 in an alkaline medium is similar to the utmost-performing electrocatalysts reported in the literature and very close to the Pt/C electrocatalysts with 20 wt% of Pt [48,105,112], thus encouraging the replacement of precious materials in AEMFCs.

In addition to appreciable selective activity, working durability must be assessed to fit the practical requirements of efficacious electrocatalysts. Therefore, accelerated stability tests (ASTs) of the best-performing electrocatalyst, i.e., cig_450, were implemented in alkaline and neutral media. The acidic electrolyte was excluded because of the lack of stability of Fe-N-C electrocatalysts attributed to the immediate demetallation, deterioration

of active sites, carbon oxidation, etc. [48]. The achieved results in neutral and alkaline media are reported in Figures S9 and S10, where cig_450 shows a continuous degradation in terms of J_{lim} in both alkaline and neutral media upon 2000 cycles while kinetics decline ($E_{1/2}$) is considerably prominent in neutral media. After 500 cycles, a pronounced degradation is observed, probably associated with the leaching of iron from exposed nanoparticles [98] or with a possible Fe dissolution/reprecipitation mechanism, which partially converts single atoms into iron oxide nanoparticles, less active than Fe centers [110]. After 2000 cycles, a J_{lim} decrease of 59% and 50% is observed in alkaline and neutral media, respectively. On the other hand, the $E_{1/2}$ shifts detected in alkaline and neutral media after 2000 cycles are 6 mV and 50 mV, respectively. From the selectivity point of view, after AST, the number of transferred electrons shifts from 3.72 to 3.52 in alkaline media while it shows a minor change in neutral media (from 3.85 to 3.81). This difference is attributed to a higher production of peroxide in the alkaline electrolyte after AST as it increases from 14 to 24%. This variation is much less prominent in the neutral environment where peroxide production grows approximatively by two units. In light of this, cig_450 should be improved from the stability point of view by optimizing the synthetic conditions during prospective endeavors.

2.3. Novelty and Perspectives

A huge amount of cigarette butts is daily discarded, thus ruining and polluting both the terrestrial and aquatic environments. Cigarette butts as a source of micro/nanoplastics, when littered into common waste streams seriously challenge the survival of the whole ecosystem. In addition, a large-scale system to collect cigarette butts is still missing, and currently, collection campaigns are mainly carried out by small clean-up crews of volunteers [113,114]. Moreover, the traditional disposal pathways mainly involve landfilling is still a direct violation of environmental safety standards due to its potential for soil toxicity. In this regard, incineration is another method that at the first glance can be considered a helpful way to generate electricity from unwanted waste, but, in reality, this practice uncontrollably releases hazardous side products and greenhouse gases into the atmosphere. On the other hand, a rational approach is to valorize the toxic wastes by converting them into a value-added product within the context of the circular economy [4,7,11,113,115]. The presented study gives a novel insight into the consumption of waste cigarette butts of negligible economic worth for the fabrication of valuable M-N-Cs for ORR electrocatalysis which is the main bottleneck in the commercialization of low-temperature FC technology. Such scientific efforts of realizing the concept of green energy by using waste products with the potential for environmental degradation will surely be an important step toward sustainability. Our results demonstrate appreciable ORR electrokinetics of the waste cigarette-derived electrocatalysts, especially cig_450, in all the three pHs that give rise to an individual class of FCs. However, this study launches an embryonic concept of using waste cigarette butts for developing M-N-C-based ORR electrocatalysts, and of course, prospective attempts should be made to further uplift the electrocatalytic performance by tailoring the suitable site structure. Moreover, M-N-Cs electrocatalysts find their demand in a broad spectrum of applications which are hotspots for scientific research such as the electrochemical reduction of carbon dioxide [116,117], nitrate reduction [118], hydrogen evolution reaction (HER) for water splitting [119–121], etc. Such kinds of M-N-Cs can be fabricated using cigarette butts as a cost-effective feedstock; however, each reaction demands proper engineering of active moieties to ensure desired activity and selectivity, which could open up a new window for future research by playing a second fiddle to the circular economy.

3. Material and Methods

3.1. Synthesis Processes

Cigarette butt waste was selectively collected from the designated cigarette receptacles installed in the smoking areas of the University of Milano-Bicocca Campus. Periodic emptying allowed the recovery of different samples, which were air-dried overnight under

a fume hood and stored in plastic bags at 20 °C. Roughly, the waste was composed of 20–25% of lignocellulosic tobacco remnants and ashes, and 75–80% of cigarettes smoked butts. In turn, cigarette butts were mainly composed of 20–25% of cellulose paper and 80–75% of cellulose acetate filters. A representative amount of cigarette butts was then washed and shredded using a commercial blender to achieve a homogeneous fluffy product including all the fractions.

The sample was pulverized using a Retsch® ball miller with ZrO_2 spheres by setting 800 rpm as rotation speed, a processing time of roughly 1 h, which was divided into intervals of 30 min alternated with a pause time of 5 min. Thereafter, about 6 g of the obtained powder was poured into an alumina boat (thermal resistance > 1700 °C), which was in turn placed in a quartz tube within Naberthem® RSH 50/500/13 tubular furnace. Prior to the instrument start-up, Ar gas was flushed for 30 min with a pressure of 100 cm^3 min^{-1} to attain an anoxic atmosphere. The pyrolysis treatment was performed starting from room temperature (r.t.) till the target temperature (450, 600, 750 or 900 °C) with a heating rate of 5 °C min^{-1}. The temperature dwelled at 900 °C for 1 h and then cooled down to room temperature at the same rate. Subsequently, the obtained char was chemically activated by using KOH with a KOH/carbon weight ratio of 4:1. First, KOH was introduced into a balloon and solubilized with absolute ethanol. Second, after the complete solubilization of KOH, char was added to the solution. The mixture was left in the capped balloon under stirring at room temperature for 24 h. Afterward, the temperature rose to 80 °C while stirring, and a constant Ar flux was flushed to let the solvent evaporate under a dry atmosphere. The dried mixture was recovered and activated in a tubular furnace. Previously, Ar was flushed for 30 min with a pressure of 100 cm^3 min^{-1} to achieve an inert atmosphere. Then, pyrolysis was carried out starting from r.t. up to 700 °C with a heating rate of 5 °C/min. The target temperature (i.e., 700 °C) was maintained for 1 h and the sample was subsequently cooled down all the way to r.t. with the same heating rate. This time, the alumina boat was lined by using a nickel strip to avoid a possible reaction of aluminum oxide with the remaining excess of KOH, and for the same reason, the tube was internally covered with a stainless-steel foil. After the activation pyrolysis, the sample was immersed in a beaker for 2–3 min with approx. 30 mL of 1 M HCl for an acid-washing process that aims at further removing KOH. The solution is then washed with milli-Q water using a vacuum flask with a Büchnell funnel until the supernatant reaches pH 7. Thereupon, the washed sample was dried in a heater for at least 5 h at 80 °C. The subsequent step was functionalization, which was accomplished by mixing the sample with 10 wt% of iron (II) phthalocyanine (FePc) in a ball miller, as previously described. Subsequently, a third pyrolysis was carried out similarly to the first pyrolysis but setting 600 °C for 1 h as a target temperature. Again, the sample was subject to further homogenization using the ball miller, as previously described, and recovered from the jar washing with absolute ethanol.

3.2. Morphological and Surface Chemistry Investigations

Thermogravimetric analysis (TGA) equipped with differential scanning calorimetry (DSC, STARe system, Mettler Toledo, Switzerland) was used to study the thermal profile of the raw material by heating the sample from room temperature to 1000 °C in a N_2 atmosphere with a heating rate of 10 °C min^{-1}. Inorganic elemental analysis was qualitatively carried out using X-rays fluorescence (XRF, Artax 200, Bruker, Billerica, MA, USA) having Mo anode. To investigate the crystallographic features, X-rays diffraction (XRD) coupled with a Cu source was employed (Rigaku Miniflex 600, Tokyo, Japan). Moreover, the carbonaceous architecture of the as-fabricated samples was studied by the means of a Raman spectroscopy (Labram, Jobin Yvon, France) assembled with a microscope (BX40, Olympus, Japan) having a Long Working Distance of 50× objective (N.A. of 0.60). For exciting the Raman samples, a helium–neon laser (wavelength of 632.8 nm) was used while the scattered signals were detected with the help of a silicon CCD functioning at 200 K (Sincerity, Jobin Yvon, France), in a backscattering mode. Raman bands were fitted as a

sum of bands with Breit–Wigner–Fano line shape to clarify the peak position, intensity and full-width half maximum, while the I_D/I_G ratio was determined by dividing the absolute band intensity of D by that of G.

Desktop scanning electron microscope (SEM, Thermo Fisher Phenom G6, Eindhoven, The Netherlands) with a thermionic CeB6 source was used to study the morphology of the prepared electrocatalysts in secondary electron (SE) mode. For further microscopic analysis, transmission electron microscopy (TEM) measurements were performed on a Thermofisher Talos F200X G2 high-resolution TEM. Images were taken at 200 kV in the HRTEM and STEM mode with a Panther detector equipped with an HAADF solid-state ring detector. EDX data, including maps, were collected with a SuperX spectrometer (Thermofisher, Waltham, MA, USA) consisting of 430 mm^2 silicon drift detectors. EDX maps were acquired with a 256 × 256 px resolution.

XPS was measured in an ultra-high vacuum chamber capable of reaching a pressure lower than 10^{-10} mbar. The radiation used was a non-monochromatized Al (hν = 1486.6 eV). The analyzer used was a hemispherical electron/ion energy analyzer (VSW with a 16-channel detector). The X-ray source had an operating power of 120 W (12 kV and 10 mA). The photoelectrons were collected perpendicularly to the surface sample in fixed analyzer transmission mode (pass energy of 44 eV). The XPS spectra calibration was conducted by setting the C1s component to 284.8 eV [122].

Sample pore architecture was evaluated by the analysis of the N_2 adsorption/desorption isotherms at 77 K, collected by an ASAP 2020 system (Micromeritics, Georgia, USA). Before measurement, the samples were dried and degassed for 24 h at 413 K. The specific surface area was quantified by the analysis of the isotherm adsorption branch according to the Brunauer–Ermett–Teller (BET) theory. Pore volume and pore size distributions were evaluated by exploiting the Density Functional Theory.

3.3. Electrochemical Characterization

The electrochemical performance was evaluated by using a three-electrode RRDE setup assembled with a Pine WaveVortex 10 rotator (USA), a Pine WaveDriver 200 EIS Biopotentiostat/Galvanostat (USA), a Pine 250 mL glass cell and a Pine rotating electrode E6R2 (USA). The inks were prepared by dispersing 5 mg of as-developed electrocatalyst in a mixture of 985 μL isopropanol (Alfa Aesar, Ward Hill, MA, USA) and 15 μL of 5 wt% Nafion® D-520 (Alfa Aesar, USA). The produced inks were sonicated for 10 min at 50% pulse amplitude. The RRDE (E6R2 series) used for the electrochemical study had a disk area of 0.2376 cm^2 with a Pt ring of 0.2356 cm^2 geometric area, while the collection efficiency (N) was 38%. Before being used, the electrode was polished on a cloth using alumina pastes to obtain a flat surface, followed by ultrasonic cleaning in water. Then, the working RRDE electrode was fabricated by drop-casting with a loading of 0.6 mg cm^{-2}. The experiments were carried out in three different electrolytes: (i) acidic solution of 0.5 M H_2SO_4, (ii) neutral solution of 0.1 M potassium phosphate buffer (PBS) and (iii) alkaline solution of 0.1 M KOH. Before beginning measurements, the cell was bubbled with pure O_2 for 30 min, and afterward, each electrocatalyst was activated through 20 cycles between the suitable potential window of the electrolyte in use at a scan rate of 100 mV s^{-1}. Linear sweep voltammetries were recorded with a rotating speed of 1600 rpm and a scan rate of 5 mV s^{-1}. A graphite rod and saturated calomel electrode (SCE) were used as a counter electrode and reference electrode, respectively. The potential window for acidic, neutral and alkaline electrolytes was maintained at +1000 to −250 mV vs. SCE (potential ring hold at 1000 mV vs. SCE), +600 to −750 mV vs. SCE (potential ring hold at 600 mV) and +150 to −1050 mV vs. SCE (potential ring hold at 150 mV vs. SCE). All measured potentials were reported with respect to reverse hydrogen electrode (RHE), to correlate it to pH, using the following relationship: E(vs. RHE) = E(vs. SCE) + 0.241 + 0.0591 pH. By monitoring the disk current

(J_{disk}) and ring current (J_{ring}), peroxide formation and electron transferred number were determined using Equations (1) and (2), respectively:

$$\% \text{ Peroxide} = \frac{200 \cdot \frac{J_{ring}}{N}}{J_{disk} + \frac{J_{ring}}{N}} \tag{1}$$

$$n = \frac{4J_{disk}}{J_{disk} + \frac{J_{ring}}{N}} \tag{2}$$

The accelerated stability tests (ASTs) were carried out with the RRDE technique by applying 2000 cycles in the potential window of 1.2 to 0 V vs. RHE at 1600 rpm and 50 mV s^{-1} in O_2^{-} saturated electrolyte. The electrocatalyst loading was maintained at 0.6 mg cm^{-2}. For comparison, LSVs at every 500th cycle were recorded at 5 mV s^{-1}.

4. Conclusions

In the framework of a circular economy, one of the most littered waste products, i.e., smoked cigarette butts, was used to develop Fe-N-C electrocatalysts via pyrolysis. The carbonaceous chars acquired at different temperatures, i.e., 450, 600, 750 and 900 °C, were activated with KOH for the inducement of porosity. Finally, the activated char was functionalized with FePc to launch active moieties for ORR. The electrochemical results were evidence of a descending trend of electrocatalytic activity with the increase in temperature pyrolysis in all three acidic, neutral and alkaline media whereas overall higher kinetic performance was obtained in alkaline electrolyte. Cig_450 outperformed the other counterparts in all three pHs by delivering the highest $E_{1/2}$ and E_{on}. The estimated values of $E_{1/2}$ and Eon for cig_450 came out to be 0.88 V and 0.5 V vs. RHE in acidic media, 0.77 V and 0.43 V vs. RHE in neutral media and 0.91 V and 0.85 V vs. RHE in alkaline media. The outstanding performance of cig_450 might be attributed to the synergic effects of optimum surface area and higher amount of Fe-N_x, ensuring a tetra-electronic process in any tested environment. Despite demonstrating excellent electrocatalytic activity, cig_450 had limited operational stability as the performance declined after 500 cycles in alkaline and neutral environments. However, this aspect can be further improved in future scientific endeavors.

Author Contributions: Conceptualization, A.F., L.Z., M.M. and C.S.; methodology, D.T., C.S., A.F., L.Z., M.M., A.L., N.L., M.A. and F.S.; formal analysis, D.T., G.Z., M.M., N.L., R.L. (Roberto Landone), A.S., R.L. (Roberto Lorenzi), E.P. and L.C.; investigation, D.T., G.Z., M.M., R.L. (Roberto Lorenzi), A.S., R.L. (Roberto Landone), E.P., L.C. and C.S.; resources, R.L. (Roberto Lorenzi), F.S., L.Z., A.F., and A.L.; data curation, D.T., G.Z., M.M., R.L. (Roberto Lorenzi), A.S., R.L. (Roberto Landone), E.P., N.L.,

References

1. Zupančič, M.; Možic, V.; Može, M.; Cimerman, F.; Golobič, I. Current Status and Review of Waste-to-Biogas Conversion for Selected European Countries and Worldwide. *Sustainability* **2022**, *14*, 1823. [CrossRef]
2. Li, J.; Song, G.; Cai, M.; Bian, J.; Sani Mohammed, B. Green Environment and Circular Economy: A State-of-the-Art Analysis. *Sustain. Energy Technol. Assess.* **2022**, *52*, 102106. [CrossRef]
3. Bhubalan, K.; Tamothran, A.M.; Kee, S.H.; Foong, S.Y.; Lam, S.S.; Ganeson, K.; Vigneswari, S.; Amirul, A.A.; Ramakrishna, S. Leveraging Blockchain Concepts as Watermarkers of Plastics for Sustainable Waste Management in Progressing Circular Economy. *Environ. Res.* **2022**, *213*, 113631. [CrossRef]
4. Marinello, S.; Lolli, F.; Gamberini, R.; Rimini, B. A Second Life for Cigarette Butts? A Review of Recycling Solutions. *J. Hazard. Mater.* **2020**, *384*, 121245. [CrossRef]
5. Araújo, M.C.B.; Costa, M.F. A Critical Review of the Issue of Cigarette Butt Pollution in Coastal Environments. *Environ. Res.* **2019**, *172*, 137–149. [PubMed]
6. Dai, X.; Gakidou, E.; Lopez, A.D. Evolution of the Global Smoking Epidemic over the Past Half Century: Strengthening the Evidence Base for Policy Action. *Tob. Control* **2022**, *31*, 129–137. [CrossRef]
7. George, M.; Khadtar, R. Review on Recycling of Microplastics in Cigarette Butts. *IOP Conf. Ser. Earth Environ. Sci.* **2022**, *1084*, 012027. [CrossRef]
8. Shen, M.; Li, Y.; Song, B.; Zhou, C.; Gong, J.; Zeng, G. Smoked Cigarette Butts: Unignorable Source for Environmental Microplastic Fibers. *Sci. Total Environ.* **2021**, *791*, 148384. [PubMed]
9. Dobaradaran, S.; Mutke, X.A.M.; Schmidt, T.C.; Swiderski, P.; De-la-Torre, G.E.; Jochmann, M.A. Aromatic Amines Contents of Cigarette Butts: Fresh and Aged Cigarette Butts vs Unsmoked Cigarette. *Chemosphere* **2022**, *301*, 134735. [CrossRef] [PubMed]
10. Farzadkia, M.; Salehi Sedeh, M.; Ghasemi, A.; Alinejad, N.; Samadi Kazemi, M.; Jafarzadeh, N.; Torkashvand, J. Estimation of the Heavy Metals Released from Cigarette Butts to Beaches and Urban Environments. *J. Hazard. Mater.* **2022**, *425*, 127969. [CrossRef]
11. Hazbehiean, M.; Mokhtarian, N.; Hallajisani, A. Converting the Cigarette Butts into Valuable Products Using the Pyrolysis Process. *Glob. J. Environ. Sci. Manag.* **2022**, *8*, 133–150. [CrossRef]
12. Xiong, S.; Peng, Y.; Chen, K.; Lu, S.; Jiang, W.; Li, X.; Wang, F.; Cen, K. Phase Distribution, Migration and Relationship of Polychlorinated Dibenzo-p-Dioxins and Dibenzofurans and Heavy Metals in a Large-Scale Hazardous Waste Incinerator. *J. Clean. Prod.* **2022**, *341*, 130764. [CrossRef]
13. van der Hulst, M.K.; Ottenbros, A.B.; van der Drift, B.; Ferjan, Š.; van Harmelen, T.; Schwarz, A.E.; Worrell, E.; van Zelm, R.; Huijbregts, M.A.J.; Hauck, M. Greenhouse Gas Benefits from Direct Chemical Recycling of Mixed Plastic Waste. *Resour. Conserv. Recycl.* **2022**, *186*, 106582. [CrossRef]
14. Ritchie, H.; Roser, M.; Rosaldo, P. Energy. Available online: https://ourworldindata.org/energy (accessed on 2 January 2023).
15. Fathy, A.; Elaziz, M.A.; Sayed, E.T.; Olabi, A.G.; Rezk, H. Optimal Parameter Identification of Triple-Junction Photovoltaic Panel Based on Enhanced Moth Search Algorithm. *Energy* **2019**, *188*, 116025. [CrossRef]
16. Konstantinidis, E.I.; Botsaris, P.N. Wind Turbines: Current Status, Obstacles, Trends and Technologies. *IOP Conf. Ser. Mater. Sci. Eng.* **2016**, *161*, 012079. [CrossRef]
17. Wilberforce, T.; El Hassan, Z.; Durrant, A.; Thompson, J.; Soudan, B.; Olabi, A.G. Overview of Ocean Power Technology. *Energy* **2019**, *175*, 165–181. [CrossRef]
18. Olabi, A.G.; Mahmoud, M.; Soudan, B.; Wilberforce, T.; Ramadan, M. Geothermal Based Hybrid Energy Systems, toward Eco-Friendly Energy Approaches. *Renew. Energy* **2020**, *147*, 2003–2012. [CrossRef]

19. Sutikno, T.; Arsadiando, W.; Wangsupphaphol, A.; Yudhana, A.; Facta, M. A Review of Recent Advances on Hybrid Energy Storage System for Solar Photovoltaics Power Generation. *IEEE Access* **2022**, *10*, 42346–42364. [CrossRef]

20. Ishaq, H.; Dincer, I.; Crawford, C. A Review on Hydrogen Production and Utilization: Challenges and Opportunities. *Int. J. Hydrog. Energy* **2022**, *47*, 26238–26264. [CrossRef]

21. Olabi, A.G.; Wilberforce, T.; Abdelkareem, M.A. Fuel Cell Application in the Automotive Industry and Future Perspective. *Energy* **2021**, *214*, 118955. [CrossRef]

22. Li, Y.; Li, Q.; Wang, H.; Zhang, L.; Wilkinson, D.P.; Zhang, J. Recent Progresses in Oxygen Reduction Reaction Electrocatalysts for Electrochemical Energy Applications. *Electrochem. Energy Rev.* **2019**, *2*, 518–538. [CrossRef]

23. Wang, Y.; Wang, D.; Li, Y. A Fundamental Comprehension and Recent Progress in Advanced Pt-based ORR Nanocatalysts. *SmartMat* **2021**, *2*, 56–75. [CrossRef]

24. He, Y.; Wu, G. PGM-Free Oxygen-Reduction Catalyst Development for Proton-Exchange Membrane Fuel Cells: Challenges, Solutions, and Promises. *Acc. Mater. Res.* **2022**, *3*, 224–236. [CrossRef]

25. Tosoni, S.; di Liberto, G.; Matanovic, I.; Pacchioni, G. Modelling Single Atom Catalysts for Water Splitting and Fuel Cells: A Tutorial Review. *J. Power Sources* **2023**, *556*, 232492. [CrossRef]

26. Arbizzani, C.; Righi, S.; Soavi, F.; Mastragostino, M. Graphene and Carbon Nanotube Structures Supported on Mesoporous Xerogel Carbon as Catalysts for Oxygen Reduction Reaction in Proton-Exchange-Membrane Fuel Cells. *Int. J. Hydrog. Energy* **2011**, *36*, 5038–5046. [CrossRef]

27. Xu, H.; Wang, D.; Yang, P.; Liu, A.; Li, R.; Li, Y.; Xiao, L.; Ren, X.; Zhang, J.; An, M. Atomically Dispersed M-N-C Catalysts for the Oxygen Reduction Reaction. *J. Mater. Chem. A Mater.* **2020**, *8*, 23187–23201. [CrossRef]

28. Wang, H.Y.; Weng, C.C.; Yuan, Z.Y. Insights into Efficient Transition Metal-Nitrogen/Carbon Oxygen Reduction Electrocatalysts. *J. Energy Chem.* **2021**, *56*, 470–485. [CrossRef]

29. Cousins, I.T.; Goldenman, G.; Herzke, D.; Lohmann, R.; Miller, M.; Ng, C.A.; Patton, S.; Scheringer, M.; Trier, X.; Vierke, L.; et al. The Concept of Essential Use for Determining When Uses of PFASs Can Be Phased Out. *Environ. Sci. Process. Impacts* **2019**, *21*, 1803–1815. [CrossRef] [PubMed]

30. Bangma, J.; Guillette, T.C.; Strynar, M.; Lindstrom, A.; McCord, J.; Hill, D.; Lau, C.; Chernoff, N.; Lang, J.R. A Rapid Assessment Bioaccumulation Screening (RABS) Study Design for Emerging per-and Polyfluoroalkyl Substances in Mice Exposed to Industrially Impacted Surface Water. *Chemosphere* **2022**, *308*, 136159. [CrossRef] [PubMed]

31. Santoro, C.; Lavacchi, A.; Mustarelli, P.; Di Noto, V.; Elbaz, L.; Dekel, D.R.; Jaouen, F. What Is Next in Anion-Exchange Membrane Water Electrolyzers? Bottlenecks, Benefits, and Future. *ChemSusChem* **2022**, *15*, e202200027. [CrossRef] [PubMed]

32. Palanisamy, G.; Jung, H.Y.; Sadhasivam, T.; Kurkuri, M.D.; Kim, S.C.; Roh, S.H. A Comprehensive Review on Microbial Fuel Cell Technologies: Processes, Utilization, and Advanced Developments in Electrodes and Membranes. *J. Clean. Prod.* **2019**, *221*, 598–621. [CrossRef]

33. Pandey, P.; Shinde, V.N.; Deopurkar, R.L.; Kale, S.P.; Patil, S.A.; Pant, D. Recent Advances in the Use of Different Substrates in Microbial Fuel Cells toward Wastewater Treatment and Simultaneous Energy Recovery. *Appl. Energy* **2016**, *168*, 706–723. [CrossRef]

34. Santoro, C.; Serov, A.; Artyushkova, K.; Atanassov, P. Platinum Group Metal-Free Oxygen Reduction Electrocatalysts Used in Neutral Electrolytes for Bioelectrochemical Reactor Applications. *Curr. Opin. Electrochem.* **2020**, *23*, 106–113. [CrossRef]

35. Katz, E.; Bollella, P. Fuel Cells and Biofuel Cells: From Past to Perspectives. *Isr. J. Chem.* **2021**, *61*, 68–84. [CrossRef]

36. Yaqoob, A.A.; Serrà, A.; Bhawani, S.A.; Ibrahim, M.N.M.; Khan, A.; Alorfi, H.S.; Asiri, A.M.; Hussein, M.A.; Khan, I.; Umar, K. Utilizing Biomass-Based Graphene Oxide–Polyaniline–Ag Electrodes in Microbial Fuel Cells to Boost Energy Generation and Heavy Metal Removal. *Polymers* **2022**, *14*, 845. [CrossRef]

37. Ghanbari, M.H.; Shahdost-Fard, F.; Salehzadeh, H.; Ganjali, M.R.; Iman, M.; Rahimi-Nasrabadi, M.; Ahmadi, F. A Nanocomposite Prepared from Reduced Graphene Oxide, Gold Nanoparticles and Poly(2-Amino-5-Mercapto-1,3,4-Thiadiazole) for Use in an Electrochemical Sensor for Doxorubicin. *Microchim. Acta* **2019**, *186*, 641. [CrossRef]

38. Santoro, C.; Bollella, P.; Erable, B.; Atanassov, P.; Pant, D. Oxygen Reduction Reaction Electrocatalysis in Neutral Media for Bioelectrochemical Systems. *Nat. Catal.* **2022**, *5*, 473–484. [CrossRef]

39. Cosenza, A.; Delafontaine, L.; Ly, A.; Wang, H.; Murphy, E.; Liu, Y.; Specchia, S.; Atanassov, P. Novel Acid-Free Process Intensification for the Synthesis of Non-Precious Metal-Nitrogen-Carbon Electrocatalysts for Oxygen Reduction Reaction. *J. Power Sources* **2023**, *556*, 232382. [CrossRef]

40. Berretti, E.; Longhi, M.; Atanassov, P.; Sebastián, D.; lo Vecchio, C.; Baglio, V.; Serov, A.; Marchionni, A.; Vizza, F.; Santoro, C.; et al. Platinum Group Metal-Free Fe-Based (Fe–N–C) Oxygen Reduction Electrocatalysts for Direct Alcohol Fuel Cells. *Curr. Opin. Electrochem.* **2021**, *29*, 100756. [CrossRef]

41. Giordano, E.; Berretti, E.; Capozzoli, L.; Lavacchi, A.; Muhyuddin, M.; Santoro, C.; Gatto, I.; Zaffora, A.; Santamaria, M. Boosting DMFC Power Output by Adding Sulfuric Acid as a Supporting Electrolyte: Effect on Cell Performance Equipped with Platinum and Platinum Group Metal-Free Cathodes. *J. Power Sources* **2023**, *563*, 232806. [CrossRef]

42. Jiang, M.; Yu, X.; Yang, H.; Chen, S. Optimization Strategies of Preparation of Biomass-Derived Carbon Electrocatalyst for Boosting Oxygen Reduction Reaction: A Minireview. *Catalysts* **2020**, *10*, 1472. [CrossRef]

43. Du, L.; Zhang, G.; Liu, X.; Hassanpour, A.; Dubois, M.; Tavares, A.C.; Sun, S. Biomass-Derived Nonprecious Metal Catalysts for Oxygen Reduction Reaction: The Demand-Oriented Engineering of Active Sites and Structures. *Carbon Energy* **2020**, *2*, 561–581. [CrossRef]

44. Li, S.; Ho, S.H.; Hua, T.; Zhou, Q.; Li, F.; Tang, J. Sustainable Biochar as an Electrocatalysts for the Oxygen Reduction Reaction in Microbial Fuel Cells. *Green Energy Environ.* **2021**, *6*, 644–659. [CrossRef]

45. Borghei, M.; Lehtonen, J.; Liu, L.; Rojas, O.J. Advanced Biomass-Derived Electrocatalysts for the Oxygen Reduction Reaction. *Adv. Mater.* **2018**, *30*, 1703691. [CrossRef]

46. Wang, M.; Wang, S.; Yang, H.; Ku, W.; Yang, S.; Liu, Z.; Lu, G. Carbon-Based Electrocatalysts Derived From Biomass for Oxygen Reduction Reaction: A Minireview. *Front. Chem.* **2020**, *8*, 116. [CrossRef] [PubMed]

47. Karimi-Maleh, H.; Karaman, C.; Karaman, O.; Karimi, F.; Vasseghian, Y.; Fu, L.; Baghayeri, M.; Rouhi, J.; Senthil Kumar, P.; Show, P.L.; et al. Nanochemistry Approach for the Fabrication of Fe and N Co-Decorated Biomass-Derived Activated Carbon Frameworks: A Promising Oxygen Reduction Reaction Electrocatalyst in Neutral Media. *J. Nanostruct. Chem.* **2022**, *12*, 429–439. [CrossRef]

48. Muhyuddin, M.; Friedman, A.; Poli, F.; Petri, E.; Honig, H.; Basile, F.; Fasolini, A.; Lorenzi, R.; Berretti, E.; Bellini, M.; et al. Lignin-Derived Bimetallic Platinum Group Metal-Free Oxygen Reduction Reaction Electrocatalysts for Acid and Alkaline Fuel Cells. *J. Power Sources* **2023**, *556*, 232416. [CrossRef]

49. Mutuma, B.K.; Sylla, N.F.; Bubu, A.; Ndiaye, N.M.; Santoro, C.; Brilloni, A.; Poli, F.; Manyala, N.; Soavi, F. Valorization of Biodigestor Plant Waste in Electrodes for Supercapacitors and Microbial Fuel Cells. *Electrochim. Acta* **2021**, *391*, 138960. [CrossRef]

50. Müller-Hülstede, J.; Schonvogel, D.; Schmies, H.; Wagner, P.; Dyck, A.; Wark, M. Incorporation of Activated Biomasses in Fe-N-C Catalysts for Oxygen Reduction Reaction with Enhanced Stability in Acidic Media. *ACS Appl. Energy Mater.* **2021**, *4*, 6912–6922. [CrossRef]

51. Fang, Y.; Wang, H.; Yu, H.; Peng, F. From Chicken Feather to Nitrogen and Sulfur Co-Doped Large Surface Bio-Carbon Flocs: An Efficient Electrocatalyst for Oxygen Reduction Reaction. *Electrochim. Acta* **2016**, *213*, 273–282. [CrossRef]

52. Zago, S.; Bartoli, M.; Muhyuddin, M.; Vanacore, G.M.; Jagdale, P.; Tagliaferro, A.; Santoro, C.; Specchia, S. Engineered Biochar Derived from Pyrolyzed Waste Tea as a Carbon Support for Fe-N-C Electrocatalysts for the Oxygen Reduction Reaction. *Electrochim. Acta* **2022**, *412*, 140128. [CrossRef]

53. Amiinu, I.S.; Zhang, J.; Kou, Z.; Liu, X.; Asare, O.K.; Zhou, H.; Cheng, K.; Zhang, H.; Mai, L.; Pan, M.; et al. Self-Organized 3D Porous Graphene Dual-Doped with Biomass-Sponsored Nitrogen and Sulfur for Oxygen Reduction and Evolution. *ACS Appl. Mater. Interfaces* **2016**, *8*, 29408–29418. [CrossRef]

54. Muhyuddin, M.; Zocche, N.; Lorenzi, R.; Ferrara, C.; Poli, F.; Soavi, F.; Santoro, C. Valorization of the Inedible Pistachio Shells into Nanoscale Transition Metal and Nitrogen Codoped Carbon-Based Electrocatalysts for Hydrogen Evolution Reaction and Oxygen Reduction Reaction. *Mater. Renew. Sustain. Energy* **2022**, *11*, 131–141. [CrossRef]

55. Muhyuddin, M.; Mustarelli, P.; Santoro, C. Recent Advances in Waste Plastic Transformation into Valuable Platinum-Group Metal-Free Electrocatalysts for Oxygen Reduction Reaction. *ChemSusChem* **2021**, *14*, 3785–3800. [CrossRef]

56. Veksha, A.; Yin, K.; Moo, J.G.S.; da Oh, W.; Ahamed, A.; Chen, W.Q.; Weerachanchai, P.; Giannis, A.; Lisak, G. Processing of Flexible Plastic Packaging Waste into Pyrolysis Oil and Multi-Walled Carbon Nanotubes for Electrocatalytic Oxygen Reduction. *J. Hazard. Mater.* **2020**, *387*, 121256. [CrossRef] [PubMed]

57. Castelo-Quibén, J.; Bailón-García, E.; Moral-Rodríguez, A.I.; Carrasco-Marín, F.; Pérez-Cadenas, A.F. Recycling and Valorization of LDPE: Direct Transformation into Highly Ordered Doped-Carbon Materials and Their Application as Electro-Catalysts for the Oxygen Reduction Reaction. *Catal. Sci. Technol.* **2022**, *12*, 1187–1201. [CrossRef]

58. Daniel, G.; Kosmala, T.; Dalconi, M.C.; Nodari, L.; Badocco, D.; Pastore, P.; Lorenzetti, A.; Granozzi, G.; Durante, C. Upcycling of Polyurethane into Iron-Nitrogen-Carbon Electrocatalysts Active for Oxygen Reduction Reaction. *Electrochim. Acta* **2020**, *362*, 137200. [CrossRef]

59. Muhyuddin, M.; Filippi, J.; Zoia, L.; Bonizzoni, S.; Lorenzi, R.; Berretti, E.; Capozzoli, L.; Bellini, M.; Ferrara, C.; Lavacchi, A.; et al. Waste Face Surgical Mask Transformation into Crude Oil and Nanostructured Electrocatalysts for Fuel Cells and Electrolyzers. *ChemSusChem* **2022**, *15*, e202102351. [CrossRef]

60. Mahto, A.; Halakarni, M.A.; Maraddi, A.; D'Souza, G.; Samage, A.A.; Thummar, U.G.; Mondal, D.; Nataraj, S.K. Upcycling Cellulose Acetate from Discarded Cigarette Butts: Conversion of Contaminated Microfibers into Loose-Nanofiltration Membranes for Selective Separation. *Desalination* **2022**, *535*, 115807. [CrossRef]

61. Blankenship, T.S.; Mokaya, R. Cigarette Butt-Derived Carbons Have Ultra-High Surface Area and Unprecedented Hydrogen Storage Capacity. *Energy Environ. Sci.* **2017**, *10*, 2552–2562. [CrossRef]

62. Masoudi Soltani, S.; Yazdi, S.K.; Hosseini, S. Effects of Pyrolysis Conditions on the Porous Structure Construction of Mesoporous Charred Carbon from Used Cigarette Filters. *Appl. Nanosci.* **2014**, *4*, 551–569. [CrossRef]

63. Zhang, W.; Wei, S.; Bai, P.; Liu, W.; Yang, C.; Xu, L. Temperature versus Type: Which Is the Determining Factor in Biomass-Based Electrocatalyst Performance? *Appl. Catal. B* **2023**, *325*, 122391. [CrossRef]

64. Elnour, A.Y.; Alghyamah, A.A.; Shaikh, H.M.; Poulose, A.M.; Al-Zahrani, S.M.; Anis, A.; Al-Wabel, M.I. Effect of Pyrolysis Temperature on Biochar Microstructural Evolution, Physicochemical Characteristics, and Its Influence on Biochar/Polypropylene Composites. *Appl. Sci.* **2019**, *9*, 1149. [CrossRef]

65. Tomczyk, A.; Sokołowska, Z.; Boguta, P. Biochar Physicochemical Properties: Pyrolysis Temperature and Feedstock Kind Effects. *Rev. Environ. Sci. Biotechnol.* **2020**, *19*, 191–215. [CrossRef]

66. Seoudi, R.; El-Bahy, G.S.; El Sayed, Z.A. FTIR, TGA and DC Electrical Conductivity Studies of Phthalocyanine and Its Complexes. *J. Mol. Struct.* **2005**, *753*, 119–126. [CrossRef]

67. de Fenzo, A.; Giordano, M.; Sansone, L. A Clean Process for Obtaining High-Quality Cellulose Acetate from Cigarette Butts. *Materials* **2020**, *13*, 4710. [CrossRef]

68. Shao, N.; Xue, F.; Hou, L.; Li, D.; Gao, Y.; Zhu, X. Effects of Ternary Potassium Containing Intumescent Flame Retardant Coating on the Combustion and Thermal Degradation Properties of Reconstituted Tobacco Sheet. *Thermochim. Acta* **2019**, *678*, 178310. [CrossRef]

69. Gaworski, C.L.; Lemus-Olalde, R.; Carmines, E.L. Toxicological Evaluation of Potassium Sorbate Added to Cigarette Tobacco. *Food Chem. Toxicol.* **2008**, *46*, 339–351. [CrossRef]

70. Yang, H.; Shang, L.; Zhang, Q.; Shi, R.; Waterhouse, G.I.N.; Gu, L.; Zhang, T. A Universal Ligand Mediated Method for Large Scale Synthesis of Transition Metal Single Atom Catalysts. *Nat. Commun.* **2019**, *10*, 4585. [CrossRef]

71. Soflaee, F.; Farahmandjou, M.; Firoozabadi, T.P. Polymer-Mediated Synthesis of Iron Oxide (Fe_2O_3) Nanorod. *Chin. J. Phys.* **2015**, *53*, 178–186. [CrossRef]

72. Pimenta, M.A.; Dresselhaus, G.; Dresselhaus, M.S.; Cançado, L.G.; Jorio, A.; Saito, R. Studying Disorder in Graphite-Based Systems by Raman Spectroscopy. *Phys. Chem. Chem. Phys.* **2007**, *9*, 1276–1291. [CrossRef]

73. Kagkoura, A.; Tagmatarchis, N. Carbon Nanohorn-Based Electrocatalysts for Energy Conversion. *Nanomaterials* **2020**, *10*, 1407. [CrossRef]

74. Xu, X.; Shi, C.; Li, Q.; Chen, R.; Chen, T. Fe-N-Doped Carbon Foam Nanosheets with Embedded Fe_2O_3 Nanoparticles for Highly Efficient Oxygen Reduction in Both Alkaline and Acidic Media. *RSC Adv.* **2017**, *7*, 14382–14388. [CrossRef]

75. Ferrari, A.; Robertson, J. Interpretation of Raman Spectra of Disordered and Amorphous Carbon. *Phys. Rev. B Condens Matter Mater. Phys.* **2000**, *61*, 14095–14107. [CrossRef]

76. Hasdeo, E.H.; Nugraha, A.R.T.; Dresselhaus, M.S.; Saito, R. Breit-Wigner-Fano Line Shapes in Raman Spectra of Graphene. *Phys. Rev. B Condens. Matter Mater. Phys.* **2014**, *90*, 245140. [CrossRef]

77. Xing, T.; Li, L.H.; Hou, L.; Hu, X.; Zhou, S.; Peter, R.; Petravic, M.; Chen, Y. Disorder in Ball-Milled Graphite Revealed by Raman Spectroscopy. *Carbon N. Y.* **2013**, *57*, 515–519. [CrossRef]

78. Artyushkova, K. Misconceptions in Interpretation of Nitrogen Chemistry from X-ray Photoelectron Spectra. *J. Vac. Sci. Technol. A* **2020**, *38*, 031002. [CrossRef]

79. Asset, T.; Atanassov, P. Iron-Nitrogen-Carbon Catalysts for Proton Exchange Membrane Fuel Cells. *Joule* **2020**, *4*, 33–44. [CrossRef]

80. Dzara, M.J.; Artyushkova, K.; Shulda, S.; Strand, M.B.; Ngo, C.; Crumlin, E.J.; Gennett, T.; Pylypenko, S. Characterization of Complex Interactions at the Gas-Solid Interface with in Situ Spectroscopy: The Case of Nitrogen-Functionalized Carbon. *J. Phys. Chem. C* **2019**, *123*, 9074–9086. [CrossRef]

81. Matanovic, I.; Artyushkova, K.; Atanassov, P. Understanding PGM-Free Catalysts by Linking Density Functional Theory Calculations and Structural Analysis: Perspectives and Challenges. *Curr. Opin. Electrochem.* **2018**, *9*, 137–144. [CrossRef]

82. Kabir, S.; Artyushkova, K.; Serov, A.; Atanassov, P. Role of Nitrogen Moieties in N-Doped 3D-Graphene Nanosheets for Oxygen Electroreduction in Acidic and Alkaline Media. *ACS Appl. Mater. Interfaces* **2018**, *10*, 11623–11632. [CrossRef]

83. Lai, L.; Potts, J.R.; Zhan, D.; Wang, L.; Poh, C.K.; Tang, C.; Gong, H.; Shen, Z.; Lin, J.; Ruoff, R.S. Exploration of the Active Center Structure of Nitrogen-Doped Graphene-Based Catalysts for Oxygen Reduction Reaction. *Energy Environ. Sci.* **2012**, *5*, 7936–7942. [CrossRef]

84. Rojas-Carbonell, S.; Artyushkova, K.; Serov, A.; Santoro, C.; Matanovic, I.; Atanassov, P. Effect of PH on the Activity of Platinum Group Metal-Free Catalysts in Oxygen Reduction Reaction. *ACS Catal.* **2018**, *8*, 3041–3053. [CrossRef]

85. Malko, D.; Kucernak, A.; Lopes, T. In Situ Electrochemical Quantification of Active Sites in Fe-N/C Non-Precious Metal Catalysts. *Nat. Commun.* **2016**, *7*, 13285. [CrossRef]

86. Chen, Y.; Huang, Y.; Xu, M.; Asset, T.; Yan, X.; Artyushkova, K.; Kodali, M.; Murphy, E.; Ly, A.; Pan, X.; et al. Catalysts by Pyrolysis: Direct Observation of Transformations during Re-Pyrolysis of Transition Metal-Nitrogen-Carbon Materials Leading to State-of-the-Art Platinum Group Metal-Free Electrocatalyst. *Mater. Today* **2022**, *53*, 58–70. [CrossRef]

87. Santoro, C.; Rojas-Carbonell, S.; Awais, R.; Gokhale, R.; Kodali, M.; Serov, A.; Artyushkova, K.; Atanassov, P. Influence of Platinum Group Metal-Free Catalyst Synthesis on Microbial Fuel Cell Performance. *J. Power Sources* **2018**, *375*, 11–20. [CrossRef] [PubMed]

88. Daniel, G.; Kosmala, T.; Brombin, F.; Mazzucato, M.; Facchin, A.; Dalconi, M.C.; Badocco, D.; Pastore, P.; Granozzi, G.; Durante, C. Highly Graphitized Fe–N–C Electrocatalysts Prepared from Chitosan Hydrogel Frameworks. *Catalysts* **2021**, *11*, 390. [CrossRef]

89. Mazzucato, M.; Daniel, G.; Mehmood, A.; Kosmala, T.; Granozzi, G.; Kucernak, A.; Durante, C. Effects of the Induced Micro- and Meso-Porosity on the Single Site Density and Turn over Frequency of Fe-N-C Carbon Electrodes for the Oxygen Reduction Reaction. *Appl. Catal. B* **2021**, *291*, 120068. [CrossRef]

90. Daniel, G.; Foltran, E.; Brandiele, R.; Nodari, L.; Pilot, R.; Menna, E.; Rizzi, G.A.; Ahmed Isse, A.; Durante, C.; Gennaro, A. Platinum-Free Electrocatalysts for Oxygen Reduction Reaction: Fe-N$_x$ Modified Mesoporous Carbon Prepared from Biosources. *J. Power Sources* **2018**, *402*, 434–446. [CrossRef]

91. Javed, R.; Khan, M.A.; Ye, D.; Zhao, Y.; Shah, L.A.; Zhang, J.; Zhao, H. Boosting Oxygen Reduction Catalysis Through Electronic Reconfiguration of Fe–N–C Induced by P Doping. *Electrocatalysis* **2021**, *12*, 747–758. [CrossRef]

92. Lv, M.; Guo, H.; Shen, H.; Wang, J.; Wang, J.; Shimakawa, Y.; Yang, M. Fe3C Cluster-Promoted Single-Atom Fe, N Doped Carbon for Oxygen-Reduction Reaction. *Phys. Chem. Chem. Phys.* **2020**, *22*, 7218–7223. [CrossRef]

93. Sgarbi, R.; Kumar, K.; Jaouen, F.; Zitolo, A.; Ticianelli, E.A.; Maillard, F. Oxygen Reduction Reaction Mechanism and Kinetics on M-N$_x$C$_y$ and M@N-C Active Sites Present in Model M-N-C Catalysts under Alkaline and Acidic Conditions. *J. Solid State Electrochem.* **2021**, *25*, 45–56. [CrossRef]

94. Bhuvanendran, N.; Ravichandran, S.; Xu, Q.; Maiyalagan, T.; Su, H. A Quick Guide to the Assessment of Key Electrochemical Performance Indicators for the Oxygen Reduction Reaction: A Comprehensive Review. *Int. J. Hydrog. Energy* **2022**, *47*, 7113–7138. [CrossRef]

95. Okonkwo, P.C.; Ben Belgacem, I.; Emori, W.; Uzoma, P.C. Nafion Degradation Mechanisms in Proton Exchange Membrane Fuel Cell (PEMFC) System: A Review. *Int. J. Hydrog. Energy* **2021**, *46*, 27956–27973. [CrossRef]

96. Du, L.; Prabhakaran, V.; Xie, X.; Park, S.; Wang, Y.; Shao, Y. Low-PGM and PGM-Free Catalysts for Proton Exchange Membrane Fuel Cells: Stability Challenges and Material Solutions. *Adv. Mater.* **2021**, *33*, 1908232. [CrossRef] [PubMed]

97. Primbs, M.; Sun, Y.; Roy, A.; Malko, D.; Mehmood, A.; Sougrati, M.T.; Blanchard, P.Y.; Granozzi, G.; Kosmala, T.; Daniel, G.; et al. Establishing Reactivity Descriptors for Platinum Group Metal (PGM)-Free Fe-N-C Catalysts for PEM Fuel Cells. *Energy Environ. Sci.* **2020**, *13*, 2480–2500. [CrossRef]

98. Muhyuddin, M.; Testa, D.; Lorenzi, R.; Vanacore, G.M.; Poli, F.; Soavi, F.; Specchia, S.; Giurlani, W.; Innocenti, M.; Rosi, L.; et al. Iron-Based Electrocatalysts Derived from Scrap Tires for Oxygen Reduction Reaction: Evolution of Synthesis-Structure-Performance Relationship in Acidic, Neutral and Alkaline Media. *Electrochim. Acta* **2022**, *433*, 141254. [CrossRef]

99. Elhenawy, S.; Khraisheh, M.; Almomani, F.; Al-Ghouti, M.; Hassan, M.K. From Waste to Watts: Updates on Key Applications of Microbial Fuel Cells in Wastewater Treatment and Energy Production. *Sustainability* **2022**, *14*, 955. [CrossRef]

100. Dhilllon, S.K.; Kundu, P.P.; Jain, R. Catalytic Advancements in Carbonaceous Materials for Bio-Energy Generation in Microbial Fuel Cells: A Review. *Environ. Sci. Pollut. Res.* **2022**, *30*, 24815–24841. [CrossRef]

101. Santoro, C.; Serov, A.; Villarrubia, C.W.N.; Stariha, S.; Babanova, S.; Artyushkova, K.; Schuler, A.J.; Atanassov, P. High Catalytic Activity and Pollutants Resistivity Using Fe-AAPyr Cathode Catalyst for Microbial Fuel Cell Application. *Sci. Rep.* **2015**, *5*, 16596. [CrossRef]

102. Mahajan, P.; Panwar, P. Perspective and Future Scope of Nanotechnology in Modification of Microbial Fuel Cell. *Mater. Today Proc.* **2022**, *71*, 179–185. [CrossRef]

103. Rojas-Carbonell, S.; Santoro, C.; Serov, A.; Atanassov, P. Transition Metal-Nitrogen-Carbon Catalysts for Oxygen Reduction Reaction in Neutral Electrolyte. *Electrochem. Commun.* **2017**, *75*, 38–42. [CrossRef]

104. Das, S.; Ghosh, S.; Kuila, T.; Murmu, N.C.; Kundu, A. Biomass-Derived Advanced Carbon-Based Electrocatalysts for Oxygen Reduction Reaction. *Biomass* **2022**, *2*, 155–177. [CrossRef]

105. Kaare, K.; Yu, E.; Volperts, A.; Dobele, G.; Zhurinsh, A.; Dyck, A.; Niaura, G.; Tamasauskaite-Tamasiunaite, L.; Norkus, E.; Andrulevičius, M.; et al. Highly Active Wood-Derived Nitrogen-Doped Carbon Catalyst for the Oxygen Reduction Reaction. *ACS Omega* **2020**, *5*, 23578–23587. [CrossRef]

106. Yang, X.; Zeng, Y.; Alnoush, W.; Hou, Y.; Higgins, D.; Wu, G. Tuning Two-Electron Oxygen-Reduction Pathways for H$_2$O$_2$ Electrosynthesis via Engineering Atomically Dispersed Single Metal Site Catalysts. *Adv. Mater.* **2022**, *34*, 2107954. [CrossRef]

107. Brocato, S.; Serov, A.; Atanassov, P. PH Dependence of Catalytic Activity for ORR of the Non-PGM Catalyst Derived from Heat-Treated Fe-Phenanthroline. *Electrochim. Acta* **2013**, *87*, 361–365. [CrossRef]

108. Ramaswamy, N.; Mukerjee, S. Influence of Inner- and Outer-Sphere Electron Transfer Mechanisms during Electrocatalysis of Oxygen Reduction in Alkaline Media. *J. Phys. Chem. C* **2011**, *115*, 18015–18026. [CrossRef]

109. Ramaswamy, N.; Mukerjee, S. Alkaline Anion-Exchange Membrane Fuel Cells: Challenges in Electrocatalysis and Interfacial Charge Transfer. *Chem. Rev.* **2019**, *119*, 11945–11979. [CrossRef]

110. Masa, J.; Zhao, A.; Wei, X.; Muhler, M.; Schuhmann, W. Metal-Free Catalysts for Oxygen Reduction in Alkaline Electrolytes: Influence of the Presence of Co, Fe, Mn and Ni Inclusions. *Electrochim. Acta* **2014**, *128*, 271–278. [CrossRef]

111. Vasiliev, V.P.; Manzhos, R.A.; Kochergin, V.K.; Krivenko, A.G.; Kabachkov, E.N.; Kulikov, A.V.; Shulga, Y.M.; Gutsev, G.L. A Facile Synthesis of Noble-Metal-Free Catalyst Based on Nitrogen Doped Graphene Oxide for Oxygen Reduction Reaction. *Materials* **2022**, *15*, 821. [CrossRef]

112. Hossen, M.M.; Artyushkova, K.; Atanassov, P.; Serov, A. Synthesis and Characterization of High Performing Fe-N-C Catalyst for Oxygen Reduction Reaction (ORR) in Alkaline Exchange Membrane Fuel Cells. *J. Power Sources* **2018**, *375*, 214–221. [CrossRef]

113. Conradi, M.; Sánchez-Moyano, J.E. Toward a Sustainable Circular Economy for Cigarette Butts, the Most Common Waste Worldwide on the Coast. *Sci. Total Environ.* **2022**, *847*, 157634. [CrossRef]

114. Ghasemi, A.; Golbini Mofrad, M.M.; Parseh, I.; Hassani, G.; Mohammadi, H.; Hayati, R.; Alinejad, N. Cigarette Butts as a Super Challenge in Solid Waste Management: A Review of Current Knowledge. *Environ. Sci. Pollut. Res.* **2022**, *29*, 51269–51280. [CrossRef] [PubMed]

115. Mirshokraee, S.A.; Muhyuddin, M.; Morina, R.; Poggini, L.; Berretti, E.; Bellini, M.; Lavacchi, A.; Ferrara, C.; Santoro, C. Upcycling of Waste Lithium-Cobalt-Oxide from Spent Batteries into Electrocatalysts for Hydrogen Evolution Reaction and Oxygen Reduction Reaction: A Strategy to Turn the Trash into Treasure. *J. Power Sources* **2023**, *557*, 232571. [CrossRef]

116. Varela, A.S.; Ju, W.; Bagger, A.; Franco, P.; Rossmeisl, J.; Strasser, P. Electrochemical Reduction of CO$_2$ on Metal-Nitrogen-Doped Carbon Catalysts. *ACS Catal.* **2019**, *9*, 7270–7284. [CrossRef]

117. Ju, W.; Bagger, A.; Hao, G.P.; Varela, A.S.; Sinev, I.; Bon, V.; Roldan Cuenya, B.; Kaskel, S.; Rossmeisl, J.; Strasser, P. Understanding Activity and Selectivity of Metal-Nitrogen-Doped Carbon Catalysts for Electrochemical Reduction of CO_2. *Nat. Commun.* **2017**, *8*, 944. [CrossRef]

118. Murphy, E.; Liu, Y.; Matanovic, I.; Guo, S.; Tieu, P.; Huang, Y.; Ly, A.; Das, S.; Zenyuk, I.; Pan, X.; et al. Highly Durable and Selective Fe- and Mo-Based Atomically Dispersed Electrocatalysts for Nitrate Reduction to Ammonia via Distinct and Synergized NO2-Pathways. *ACS Catal.* **2022**, *12*, 6651–6662. [CrossRef]

119. Baghban, A.; Habibzadeh, S.; Zokaee Ashtiani, F. On the Evaluation of Hydrogen Evolution Reaction Performance of Metal-Nitrogen-Doped Carbon Electrocatalysts Using Machine Learning Technique. *Sci. Rep.* **2021**, *11*, 21911. [CrossRef]

120. Wang, Y.; Cui, X.; Peng, L.; Li, L.; Qiao, J.; Huang, H.; Shi, J. Metal–Nitrogen–Carbon Catalysts of Specifically Coordinated Configurations toward Typical Electrochemical Redox Reactions. *Adv. Mater.* **2021**, *33*, 2100997. [CrossRef]

121. Morozan, A.; Goellner, V.; Nedellec, Y.; Hannauer, J.; Jaouen, F. Effect of the Transition Metal on Metal–Nitrogen–Carbon Catalysts for the Hydrogen Evolution Reaction. *J. Electrochem. Soc.* **2015**, *162*, H719–H726. [CrossRef]

122. Miller, D.J.; Biesinger, M.C.; McIntyre, N.S. Interactions of CO_2 and CO at Fractional Atmosphere Pressures with Iron and Iron Oxide Surfaces: One Possible Mechanism for Surface Contamination? *Surf. Interface Anal.* **2002**, *33*, 299–305. [CrossRef]